Systematic Investigation of Defect-Mediated Photoluminescence Through Radiation-Induced Displacement Damage

BY

Sarah L. Gollub

Dissertation

Submitted to the Faculty of the

Graduate School of Vanderbilt University

in partial fulfillment of the requirements

for the degree of

DOCTOR OF PHILOSOPHY

in

Interdisciplinary Materials Science

May, 2015

Nashville, Tennessee

Approved by:

Professor Greg Walker, Chair

Professor Bridget Rogers

Professor Richard Haglund

Professor Ronald Schrimpf

Professor Robert Weller

ACKNOWLEDGMENTS

Funding was provided by the Defense Threat Reduction Agency (DTRA Grant HDTRA1-10-1-0112) and the Vanderbilt Institute of Nanoscale Science and Engineering (VINSE).

The work presented here and as a result of my efforts in graduate school exist because of the support and guidance of my advisor Greg Walker. His excitement and curiosity about scientific research inspire me to question what I know and pursue answers, even if there may not be a "right" answer. Dr. Walker's belief in my abilities helped me to overcome many of the challenges I encountered in school. In addition to his guidance in academics, he has become a personal friend and mentor whose opinions and advice I value and respect. I will treasure our friendship forever.

I want to acknowledge my committee members Dr. Bridget Rogers, Dr. Ronald Schrimpf, Dr. Richard Haglund, and Dr. Robert Weller for their input and support on my work. Having professors from different disciplines gave me the opportunity to learn and apply ideas in a unique way–one that contributes to our understanding of science.

I am grateful for my friends in Nashville, particularly the runners, who listened and encouraged me every step of the way. Many of them shared their experiences from graduate school and helped me feel like less of an imposter. Once again, other's beliefs in me helped me believe in myself.

Lastly, I want to express my deepest gratitude for my family and fiancé. My family has supported, encouraged, and inspired my quest for knowledge my entire life. I feel incredibly privileged to have been given opportunities to learn. Not only to learn–but to create and share knowledge. Danny has been my column of strength for more than just the years in Nashville. Danny has an unquenchable desire to do whatever it takes to help me accomplish my goals. He also gets me to do what I don't want to do, but need to do. I am so lucky to have him and I cannot wait to spend the rest of our lives together.

TABLE OF CONTENTS

LIST OF FIGURES

LIST OF TABLES

NOMENCLATURE

UV	ultraviolet
VIS	visible
FRET	Förster or Fluorescence Resonant Energy Transfer
Y_0	overall yield of unirradiated sampled (N=0)
τ	lifetime (s)
t	time (s)
I	intensity (a.u.)
I_0	initial intensity (a.u.)
$\frac{I}{I_0}$	relative light emission
N	total number of particles$/\,\mathrm{cm}^2$ striking the crystal (dose)
A	fitting parameter = half-brightness dose ($N_{1/2} = 10^{-11}$)
x_a	concentration of sites being occupied by an activator
d	energy transfer distance
τ_r	lifetime via radiative emission
τ_d	lifetime via quenching by defects
τ_a	lifetime via quenching by activator pairs
τ_{th}	lifetime via thermal quenching
E	FRET efficiency
r	distance between donor and acceptor
R_0	distance between two dipoles when transfer efficiency = 50%
Q_0	fluorescence quantum yield
κ^2	dipole orientation factor
n	index of refraction
N_A	Avogadros number, 6.02214×10^{23}
J	spectral overlap integral
f_D	normalize donor emission
ε_A	acceptor molar extinction coefficient
α	excitation efficiency
ρ	reflectivity
$I_{\lambda m}$	spectral intensity of emission
$I_{\lambda r}$	spectral intensity of reflected light
q	quantum yield
σ_x	standard deviation of peak
μ_x	center of peak
R/O	ratio of red to orange emission peaks

CHAPTER I

INTRODUCTION

Phosphors are often used as radiation indicators because they emit light when exposed to ionizing radiation. A charged particle, upon interaction with the phosphor material, will excite electrons. Relaxation of the electrons usually results in photon emission, and characterization of that emission tells us about the nature of the interaction. Instead of creating emission from ionizing radiation, our project leverages photoluminescence emission to query radiation-induced displacement damage. Displacement damage was created in the material using particle radiation. Compared to the ephemeral emission form ionization (called scintillation), which is gone moments after the exposure is removed, displacement damage is essentially permanent. Consequently, the material that has been damaged by radiation can be queried at any arbitrary time after the irradiation, and the effects of the damage are effectively recorded into the material resulting in a remotely readable, permanent record of the radiation exposure.

The approach to determine whether non-ionizing radiation causes displacement damage in phosphors included systematically exposing several materials to x-rays, alpha particles, protons, and neutrons. Since phosphor luminescence intensity and lifetime are mainly governed by the arrangement of luminescent centers in the host lattice and the local crystal environment of each luminescence center, the optical properties were used to quantify changes in the local crystal structure. Instead of measuring the scintillation light yield, the photoluminescence spectrum and lifetime were measured. In this work, scintillation refers to the emission during irradiation and photoluminescence refers to the emission from a UV-VIS source or a laser after irradiation. The results of these experiments provide insight into the possible mechanisms of damage and instruct how to design a material with

the desired interaction effects with radiation exposure.

The materials selection was motivated in part by the ultimate goal of the research, which was to identify materials that would react with neutrons to create a permanent record of radiation exposure. The first material tested was $Y_3Al_5O_{12}$ (YAG) because it has been well-studied and thus has a heavy presence in the literature and because our lab group has experience with the material. We used this as a screening material, but ultimately, the aluminum was replaced with boron because ^{10}B is known to have a large neutron cross section [4], which should increase the probability of radiation interactions. Unfortunately, boron does not substitute equivalently for the aluminum and the crystal structure of the two materials is quite different. Nevertheless, the structure of the luminescence spectra, which is one method used to indicate damage, is similar.

Not only were multiple types of phosphors synthesized and irradiated, but also multiple fabrication studies were performed to enhance the emission intensity of the phosphors tested. Some of these fabrication studies were performed by Robert Harl and Courtney Mitchell from the Roger's group. These experiments were necessary because the concentration of rare-earth activator needed for maximum emission intensity depends on the host lattice. For example, when cerium is the dopant in a phosphor, the most intense emission usually results with a doping concentration around 1% or less. The concentration of europium, on the other hand, usually needs to be much greater, sometimes as high as 20% [5]. Regardless of the emission intensity, the material sensitivity to radiation damage can be affected by the doping concentrations, and thus a range of doping concentrations were explored during the radiation experiments.

In addition to choosing a material, a robust protocol for experimentation was necessary. To determine whether the changes in the spectra and decay were due to irradiation and not from contamination or inconsistent data collection, etc., it was important to develop a reliable approach to preparing samples and performing spectroscopy and lifetime measurements. We resolved issues with how the samples were mounted and took steps to

ensure that the same spot was queried before and after the exposure.

By deconvoluting the emission spectra with Gaussians, we were able to normalize emission with the integral of the reflected excitation peak for consistent comparison between samples. By fitting exponentials to the entire decay trace, we were able to determine the lifetime of the material without choosing an arbitrary range to fit a line and calculate τ, which is common among lifetime data reduction techniques. This approach also allowed us to examine multiple decay mechanisms. The phenomenological model described by Birks and Black was used to represent the emission degradation with radiation exposure. Furthermore, the decay trends of irradiated samples were fit using a model motivated by Dexter. These models help to distinguish between influences from various quenching mechanisms that affect the lifetime. This work concludes with remarks about the relationships between activator concentration, lifetime, and proton fluence that are new to the scientific community.

Also included are experiments and results from collaborative works on YAG:Dy and YAG:Tm as high-temperature thermographic phosphors. Controlled calibration experiments were performed, and the data were used as a standard to compare for other high temperature environments. YAG:Tm is a good candidate because it has an emission line at a shorter wavelength than other high-temperature thermographic phosphors, and thus can be detected even when black-body radiation obscures the other emission wavelengths.

1.1 Applications

Rare-earth orthoborates are particularly suited for applications such as flat panel displays and fluorescent lighting [6] because of their VUV transparency [7] and exceptionally high damage threshold [8]. Studies of these materials are often focused on fabrication because the light output is strongly dependent on the bulk configuration [9] (powder vs. crystal, for example). Other studies have focused on the conversion efficiency useful for silicon solar cells [10] or properties and structure suitable for optoelectronic devices [11, 12].

These materials have also been used as scintillators for radiation detection [13, 14] where the luminescence intensity is measured as a function of radiation dose.

The most researched property is scintillation—the immediate emission of photons upon absorption of energy. Scintillation is caused by an electron, an alpha-particle, an ion, or a high-energy photon. Efficient scintillators have a fast de-excitation (returning to the ground state), high light output, and are transparent to their own emission. Solid-state lighting, light emitting diodes (LEDs), and incandescent lamps use a type of scintillation called electroluminescence, where the emission of light is a result of electric current. Fluorescent lamps use electricity to ionize a gas inside the bulb (typically mercury) which in turn causes electrons to be excited and scattered. These electrons hit a layer of phosphors deposited on the inside of the bulb and excite their electrons, which emit photons upon relaxing back to the ground state. Although phosphors were used in cathode ray tubes (CRT) in televisions and computers, plasma display panels (PDPs) have mostly replaced them. PDPs are display devices consisting of pixels, which radiate light directly or emit luminescence from phosphors. The phosphors are excited by ultraviolet light that is produced by a gas discharge. These screens require multiple colors, so more than one phosphor is needed to produce different colors of light. For example, $Sr_3(PO_4)_5Cl:Eu^{3+}$ emits in the blue, $LaPO_4:Ce^{3+}$ emits in the green, and $Y_2O_3:Ce^{3+}$ emits in the red. The combination of certain phosphors creates emission of various colors, including nearly white light.

Γ-ray cameras (Auger cameras) take pictures of emitted isotopes in the human body, usually with $NaI:Tl^{+}$ phosphors. More common, however, are X-ray computed tomography (CT) scans. X-rays attenuate as they pass through the body and then hit a phosphor film (usually CsI:Na) that scintillates. This input film is also layered with indium oxide and a photocathode where the photons are converted to photoelectrons. The photoelectrons from this film travel through a vacuum and electron optics where they are accelerated into another phosphor film that captures the image.

Another common application is phosphor thermometry [15, 16]. Phosphor ther-

mometry is a technique for temperature measurement which utilizes the decay time of the phosphor [17]. Phosphor temperature dependence can be manipulated by the type of elements in the phosphor. For example, YAG:Dy has a very high temperature range sensitivity (above 1200°C) [18], whereas La_2O_2S:Eu is sensitive down to cryogenic temperatures. Phosphor thermometry is useful for measuring temperatures of moving parts or of places that are difficult or impossible to get to with a thermocouple.

1.1.1 Activator Selection

Cerium(III) in YBO_3 emits two broad peaks centered around 388 nm and 412 nm. There is also a weaker peak from cerium 4+ around 450 nm that appears when higher concentrations of cerium are doped in YBO_3. Emission from cerium is a 5d-4f transition. Because the 5d levels are not shielded (as the 4f levels are) they interact strongly with the local crystal and vibronic states. Therefore, transitions from $5\,d-4f$, which are allowed, are broad. Therefore, the emission spectrum is narrow. These emission peaks largely overlap each other, and the 388 nm peak overlaps the reflection of the excitation at 365 nm. These two emission peaks occur because the crystal lattice of YBO_3 creates a 5d energy level state. From this state, energy can transition to the relaxed states at the $^2F_{5/2}$ and $^2F_{7/2}$. These transitions emit energy approximately equal to 3.2 eV (388 nm) and 3 eV (412 nm) as photons. YBO_3:Ce^{3+} has a lifetime on the order of 30 ns. If the lattice is disturbed, the 5d level may be at a different energy and thus the transition energies change as well. This results in shifting of the emission peaks to correspond with the energy transition levels.

Although the crystal's influence on the 5d level provides a Stokes shift in the visible region in YAG:Ce^{3+}, the amount of cubic symmetry around the ion is responsible for the precise emission wavelength [19]. As the dopant atoms are substituted for Al (i.e. Ga) the local structure becomes more symmetric [20]. Consequently, the emission red-shifts. If the local environment is altered by radiation damage, we hypothesize that the emission could shift. . Europium(III) in YBO_3 emits at least three peaks: 593, 611, and 627 nm. Europium

transitions all occur in the 4f-4f levels. They are forbidden, and do not interact with the crystal because they are shielded. Unlike the cerium emission, europium peaks are narrow and separated, overlapping only slightly at the tails. Europium emission is not sensitive to the crystal lattice the way cerium is because the excited energy level ($^5D_0$) exists regardless of the lattice structure. However, the number of transitions which occur in Eu^{3+} depends on the crystal field. This means that there can be as many as six peaks in the spectrum of a europium-doped phosphor. Europium tends to have a longer lifetime than cerium. The lifetime of europium in YBO_3 is on the order of 4 ms [21] whereas the lifetime of cerium in $YBO_3$is on the order of 30 ns. While the peaks in a cerium-doped material shift when the lattice is disturbed, the peaks of a europium-doped material do not. Instead, the crystal field may be affected resulting in splitting and therefore more emission peaks.

CHAPTER II

BACKGROUND

2.1 General

Phosphors are materials that luminesce or give off light upon absorbing energy. Since phosphors have been known for so long, the terminology describing them has changed over time. The root of luminescence is "lumin," which means "light." However, fluorescence, phosphorescence, and photoluminescence are also commonly used terms to describe the same process.

Phosphors are crystals composed of a host lattice and an impurity, usually an activator ion. While the composition of the host lattice is varied and includes borates and phosphates, etc., the activator is usually a lanthanide or rare-earth element. Sometimes, an additional impurity ion is added as a sensitizer that enhances the emission intensity of the activator by transferring energy to the activator.

Phosphor luminescence can be stimulated with different types of energy. Furthermore, the terms for the resulting luminescence may have multiple names. Photoluminescence generally indicates light (photons) as the energy source absorbed by the material. Triboluminescence results from friction. Chemiluminescence is produced by a chemical reaction that creates the emission (glow-sticks, for example). Thermoluminescence occurs when the energy absorbed is heat. Bioluminescence is emission from a living organism. Cathodoluminescence occurs when electrons are the excitation energy. These terms refer to the type of energy that excites the phosphor.

Although radiative emission is always light, the emission spectrum may be different depending on the source of excitation energy. For example, the emission spectrum produced by fracture (triboluminescence) may not be equivalent to the emission spectrum

produced when the same material is excited by UV light [22]. In this review, the emission measured during excitation by any source other than the UV source is "scintillation," and the "photoluminescence" is measured during excitation from the UV source. This means that the emission during radiation experiments is considered scintillation.

The properties of phosphors are sensitive to the method of synthesis and processing—the crystal size, activator (dopant) concentration, post-processing (annealing) temperature, and form of the final product (powder, solid, film, etc.). A nanoparticle phosphor with 1% activator concentration could demonstrate very different spectral properties and lifetime than the same phosphor as a single crystal with 5% activator concentration. Furthermore, interactions with radiation could be more or less sensitive. This variability makes phosphors a useful material that can be fabricated to perform as desired.

2.2 Synthesis

There are many types of phosphor synthesis. Synthesis techniques include sol-gel [5], hydroxide precipitation, hydrothermal synthesis [23, 24], solid-state reaction [25, 26], and combustion synthesis [9]. Our fabrication method is a gel-combustion technique which produces a powder. Each synthesis has techniques and variables that can be altered to produce the same basic material, but with different properties. Variables include the starting reagents (powder, liquid, solution, etc.), temperature during processing, temperature post-processing, volume of material fabricated, duration of processing, tools used, conditions during synthesis (under vacuum, Argon instead of air, etc.). These variables can affect the formation of the crystals–speed, size, distribution, which in turn can affect the properties of the material. For our experiments, we made phosphors with three host lattices: YAG, LZO, and YBO_3. We doped these lattices with either Ce^{3+}, Eu^{3+}, or both.

Cerium(III) is an especially desirable dopant for luminescence because of its high light yield, fast response time (10-100 ns), easy fabrication, and low cost. More importantly, because of the crystal field and the spin-orbit coupling of the 5d electron, the Ce^{3+}

excitation energy is dependent on its crystalline host lattice. The absorption of Ce^{3+} can be around 470 nm in YAG or as low as 280 nm in $LaCl_3$. Furthermore, the emission is also variable, ranging from 540 nm in YAG:Ce^{3+} to 350 nm in $LaCl_3$:Ce^{3+} [27]. The emission is always composed of a two-peak broadband spectrum because the 4f electrons of Ce^{3+} always split into $^2F_{5/2}$ and $^2F_{7/2}$ which do not depend on the crystal environment.

Europium (III) is another common dopant used in phosphor applications, particularly for its red emission. However, unlike Ce^{3+}, Eu^{3+} emits multiple sharp peaks and a much greater dopant concentration is required for a high light yield. Europium has many $^5D_0 \longrightarrow {}^7F_J$ transitions (where J=1, 2, 3, 4...). Although europium has multiple transitions, none result directly from the crystal environment. We normally see crystal field splitting of certain levels when the europium is placed in a lattice, and the strength of the splitting between magnetic and electronic transitions is heavily dependent on the local crystal field. If the local crystal field becomes disturbed, as in radiation damage, then we would expect a corresponding change in the luminescent spectrum.

2.2.1 YAG

$Y_2O_3-Al_2O_3$ can exist in three different crystal phases: $YAlO_3$ which is a perovskite structure called YAP, $Y_4Al_2O_9$ which is a monoclinic structured called YAM, and $Y_3Al_5O_{12}$ which is a cubic garnet structure called YAG shown in Figure 2.1. YAG is often used in solid-state lasers with erbium or neodymium. When cerium is substituted for yttrium, it becomes the brightly emitting phosphor in the form of $Y_{3-x}Al_5O_{12}$:Ce_x. YAG:Ce^{3+} is commonly used in a variety of lighting applications–LEDs, cathode ray tubes, mercury-vapor lamps, etc. YAG:Ce^{3+} can also be doped with gadolinium resulting in $Y_{3-x}Al_{5-y}O_{12}$:Ce_x,Ga_y and blue-shifting the emission spectrum [28].

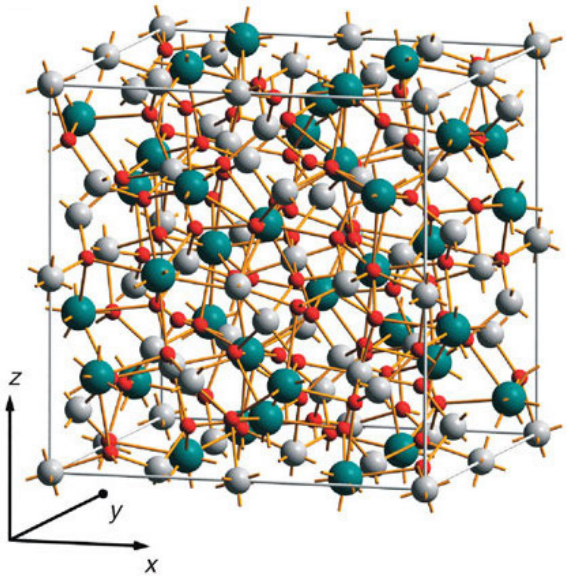

Figure 2.1 The unit cell of YAG, where green represents the yttrium, white represents aluminum, and red sites represent oxygen [1].

2.2.2 LZO

Lanthanum zirconate (LZO) is a pyrochlore which luminesces when doped with a rare-earth compound. Pyrochlores take the chemical form $A_2B_2O_7$, where the A=Y, La, Nd, Sm, Eu, or Gd and B=Ti, Zr, Hf, or Sn. See Figure 2.2. In this case we use $La_{2-x}Zr_2O_7{:}Eu_x$ where x=0.01, 0.02, 0.03, 0.04, or 0.05. We used 5% Eu^{3+} for most radiation experiments to enhance the intensity of the emission.

2.2.3 YBO_3

The crystal structure of YBO_3 has been debated many times, but most sources suggest a hexagonal vaterite-type structure with a $P6_3/m$ space group. However, a study by Lin et al. used neutron diffraction to study the transition phases of $LnBO_3$. They looked at the low-temperature and high-temperature morphology of $Y_{0.92}Eu_{0.08}BO_3$ and ultimately concluded that a better space group assignment for vaterite-type YBO_3 is $C2/c$ with unit cell

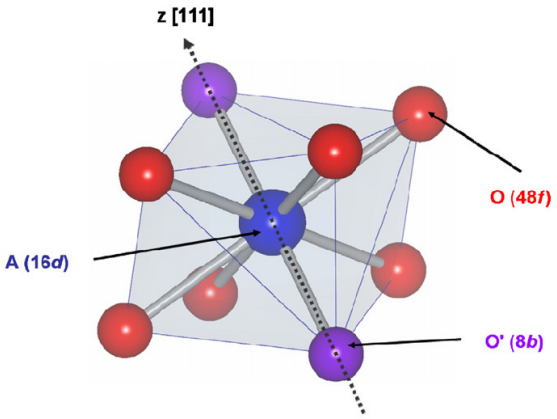

Figure 2.2 The coordination geometry of A ions in the pyrochlore structure [2].

parameters $a = 11.3138(3)$ Å, $b = 6.5403(2)$ Å, $c = 9.5499(2)$ Å, and $\beta = 112.902(1)^\circ$. A 2007 study by Li et al. agrees with this conclusion [29].

Boron-10 has a large neutron radiation cross-section, meaning it should be more susceptible to damage from neutrons than a phosphor without it.

2.2.4 Europium Tetrakis

Europium tetrakis dibenzoylmethide triethylammonium (EuD_4TEA) is a triboluminescent material with an extremely high light yield. Triboluminescence is the ability to emit light when the material's crystals fracture. It is easy to fabricate, and when the material loses the ability to fracture any further, it can be dissolved back into ethanol and the crystals regrown.

2.3 Photoluminescence Spectroscopy

The optical spectrum measured during excitation by electrons, for example, may differ from the spectrum measured by another UV excitation. Furthermore, the terminology of which spectral data being analyzed may be unclear in the literature. For example, the

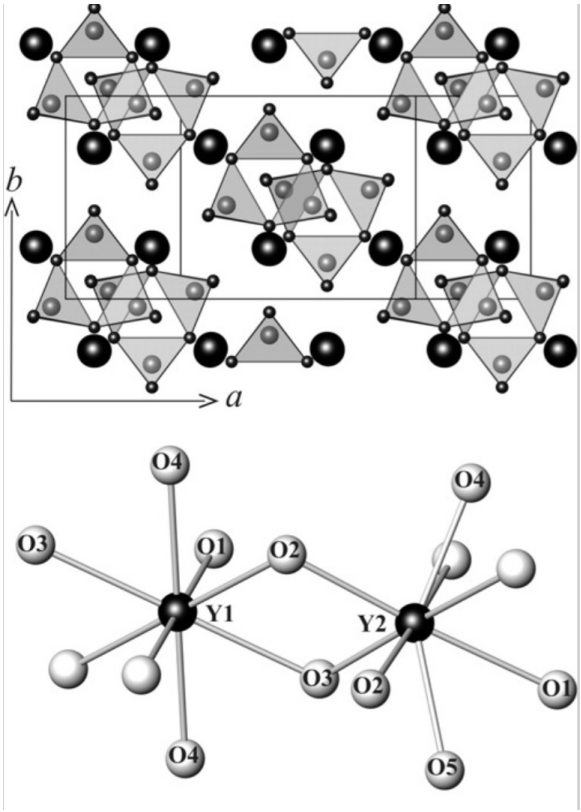

Figure 2.3 Projection of the structure of the low-temperature phase $Y_{0.92}Er_{0.08}BO_3$ along the (001) direction, and coordination polyhedra of Y1 and Y2 atoms [3].

luminescence that results from excitation of a phosphor during charged particle bombardment may produce a different spectrum than, all variables remaining the same, excitation with a UV-VIS source. Some scientists may call this particle-induced luminescence (PIL) and optically-stimulated luminescence (OSL), respectively, or perhaps just scintillation and photoluminescence.

The Birks and Black model [30] is used for scintillation luminescence to obtain an estimate of the half-brightness radiation dose for materials from measured emission. This parameter indicates the sensitivity of the material to radiation-induced changes in the scintillation. Here we consider scintillation to be the light output during particle irradiation, or electroluminescence. For our case, we are interested in the photoluminescence *after* the material has been exposed (not during) and so we distinguish the light output from photo-excitation from the scintillation or the light output from proton-excitation. Despite this distinction, we can apply the Birks and Black model, being phenomenological in origin, to indicate the sensitivity of the photoluminescence to radiation-induced displacement damage as well.

$$\frac{Y}{Y_0} = \frac{1}{1+N/A}, \tag{2.1}$$

where N is the total number of particles per area striking the crystal (dose), Y_0 is the overall yield of the un-irradiated sample ($N = 0$), and A is a fitting parameter that represents the half-brightness dose.

2.4 Decay

The duration of the emission of light depends on the material. Emission lifetime, also called the decay, can range from nanoseconds to seconds. Glow in the dark toys have an especially long lifetime, lasting for hours. Dye-pumped lasers are often made with phosphors like YAG:Dy to produce very brief powerful bursts of light. Although all phosphors have an emission lifetime, some lifetimes can be affected by external events

such as heat or radiation.

Phosphor lifetimes decrease with increasing temperature. The rate of decrease is unique to each phosphor. The intensity of luminescence decays exponentially

$$I = I_0 e^{-t/\tau} \tag{2.2}$$

where I_0 is the initial intensity, t is time, and τ is the temperature-dependent lifetime. The lifetime of bulk YBO_3:Eu^{3+} phosphors is approximately 4.73 ms [31] whereas the lifetime of YBO_3:Ce^{3+} is about 30 ns [25].

2.5 Radiation

The two main types of radiation are ionizing and non-ionizing. Ionizing radiation uses the kinetic energy of a particle to release an electron from an atom or molecule. Directly ionizing radiation includes alpha and beta particles. Protons, neutrons, gamma rays, and x-rays are indirectly ionizing. At high fluences, it may be possible to permanently damage a phosphor with ionizing radiation, but our prior work has not been able to confirm this because the resources available at Vanderbilt have relatively low activity and thus experiments take a long time.

2.6 Literature Review - Radiation Studies

Using phosphors for radiation detection typically utilizes scintillation. The phosphors are excited by ionizing radiation or thermal stimulation (thermostimulatied luminescence), but not often used to detect non-ionizing radiation.

Some of the first radiation studies using phosphors trace back to the 1950's when J.B. Birks and F.A. Black measured the scintillation efficiency of anthracene exposed to alpha-particle radiation [30]. Using a polonium source, they exposed a small crystal to

50 hours with a flux of $1.1 \times 10^9\,\alpha$ particles/cm^2/minute. They measured the amplitude of the scintillation of the anthracene intermittently using a PMT. From this, they were able to develop a model, see Equation 2.1, that matched the phenomenological results of the degradation of emission intensity due to the radiation exposure. Two weeks after the irradiation, the anthracene had not recovered its original fluorescence efficiency–the damage was permanent. Birks and Black attributed this damage to "intense ionization" [30].

Hollerman et al. have numerous works published about the scintillation response of various phosphors to proton radiation. Several of their studies were funded for space-based applications seeking materials resistant to ionizing radiation or materials that could anneal and self-repair from ionizing radiation [32–34]. Their works examine phosphor fluorescence from proton beams at 3 MeV [34, 35, 35–38] and 45 MeV [39]. The phosphors were tested as films mixed with binders. The effects of the radiation damage were examined as a function of luminescence intensity, specifically, the dose required to reach half-brightness, during the irradiation, but the post-radiation exposure emission or lifetime were not examined [34, 38, 39]. Although Hollerman et al. have done extensive work with the scintillation response of various phosphors to proton irradiation, and their work provides an indication of which materials are more susceptible to radiation damage, they do not explore the mechanism(s) of damage.

Gaubas et al. investigated luminescence characteristics during 1.6 MeV proton bombardment of polycrystalline CdS [40]. They evaluated the defect introduction rate by examining both laser- and proton-induced luminescence, but focused on the emission and did not consider the lifetime.

Kortov recently wrote a summary entitled "Modern trends and development in high-dose luminescent measurements" [41], which explains that high-dose dosimetry materials need to be radiation-resistant so that the luminescent centers do not degrade under intensive irradiation. Kortov suggests that nanostructured phosphors are prime candidates for high-

dose thermoluminescent dosimetry because they have a large capacity for trapping centers. Kortov discusses why nanostructured ceramics are particularly promising; annealed to remove charge defects so that they can be reused.

There are various other studies which address phosphor luminescence affected by ionizing radiation or thermal neutrons [42–49], yet most of these studies look exclusively at the scintillation during irradiation.

In the literature, displacement damage from non-ionizing radiation is mostly associated with silicon devices, semiconductors, and other microelectronics. There are studies that investigate damage constants and light outputs of LEDs [50–52]. There is still a gap in the understanding of how optical properties of phosphors, photoluminescence and decay especially, are affected by non-ionizing radiation.

2.7 High-temperature Thermography

Thermographic phosphors are often used to measure temperatures in harsh thermal environments because of their non-contact nature, chemical and thermal robustness, and independence on radiative properties [15]. Because spectral emission from the visible region is used to indicate temperature, black-body radiation from high-temperature surfaces can obscure the measurement signal. The 365 nm emission line in thulium-doped YAG could be used in high-temperature measurements because its wavelength is significantly shorter than other emission lines in common high-temperature phosphors. Although the intensity of the emission peak is somewhat lower than the other characteristic lines in YAG:Tm, the lifetime is measurable and shows a strong dependence on temperatures above 900°C. Gated spectral measurements help identify energy levels responsible for the 365 nm emission.

YAG:Tm has been identified as a possible candidate for remote high-temperature measurement [53]. The material's chemical robustness and high-temperature survivability make it suitable for applications like combustion environments where harsh thermal conditions would destroy traditional sensors. We are interested in this particular material because

it has an emission line at 365 nm, which is shorter in wavelength than many other high temperature emission lines in other materials such as YAG:Dy [54]. This UV emission peak is important in applications where black-body radiation can obscure long wavelength spectral emissions. Although this short wavelength emission peak at 365 nm has been identified before [55], its temperature dependence has not been studied and that is the focus of the present effort.

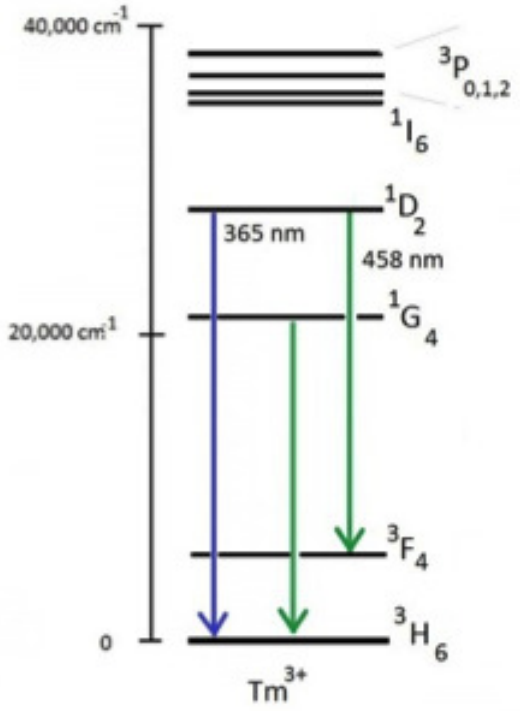

Figure 2.4 Energy level diagram of Tm^{3+}.

The activator Tm presents a variety of energy levels resulting in a rich spectrum. Figure 2.4 is a simplified energy level diagram showing the higher levels. Of primary

interest is the $^1D_2$ state but the levels above this are also of potential for high temperature applications and should be addressed in future work. Guy [56] provided information on the dynamics of higher states in YAG:Tm for $^1I_6$, $^1D_2$, and $^1G_4$. For the example of a crystal of 0.1 atomic percent at 10 K, the decay times are $37 \pm 2\,\mu$s, $50 \pm 2\,\mu$s, and $570 \pm 10\,\mu$s, respectively. These values change with dopant concentration and morphology but are a guide as to what to expect.

To our knowledge, the first to exploit Tm for fluorescence thermometry was Zhang [53, 57]. Temperature dependence from ambient to 1350°C was observed of infrared bands longer than 1 μm from the $^3H_4$ and $^3F_4$ states. The material was in the form of a YAG:Tm optical fiber where the fluorescent emission is confined inside the fiber. In that case, the ratio of the signal to blackbody radiation is larger than for thin phosphor coatings in non-contact applications under consideration here. Cates [18] monitored emission from $^1D_2$ at 458 nm from a phosphor powder sample of YAG:Tm, observing fluorescence to 1500°C. For phosphor thermometry, monitoring shorter wavelength emission bands may be advantageous since blackbody emission decreases with wavelength. This is illustrated by Figure 2.5 where blackbody emission curves for 1200 and 1400°C are plotted along with an emission spectrum of YAG:Tm. Blackbody emission decreases by factors of 60 and 40 from 458 to 365 nm at these two temperatures respectively.

2.8 Mechanisms

There are two mechanisms of emission: radiative and non-radiative. Radiative emission occurs when energy absorbed by the host lattice excites the activator to a higher energy state and the activator emits that energy in the form of a photon as it drops back down to its ground state. Non-radiative emission occurs when the energy absorbed by the host lattice is either too little to excite the activator, or is just absorbed within the lattice and dissipated as phonons—also called quenching. However, there are several other steps that can occur after the absorption of excitation energy but before either emission or quench-

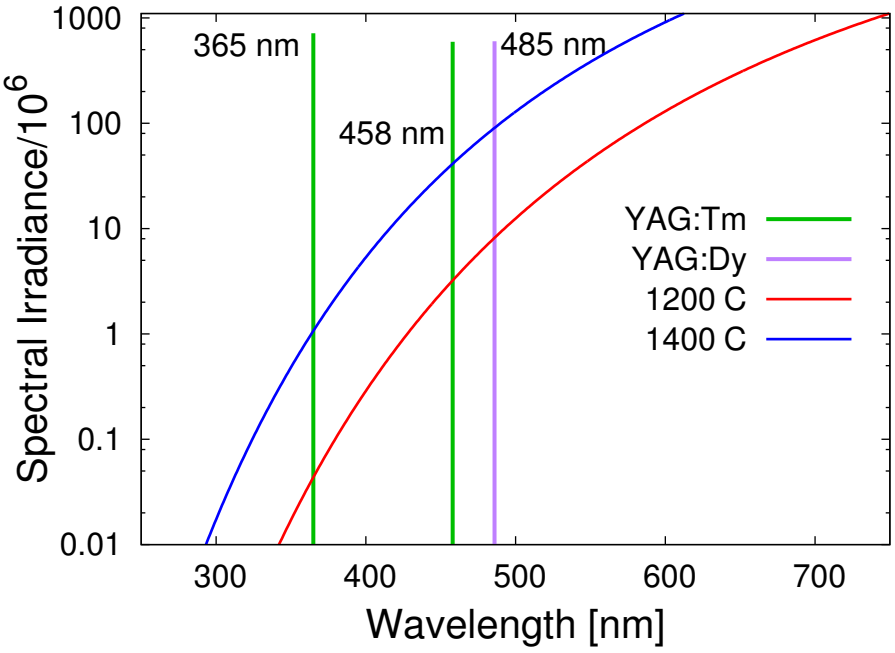

Figure 2.5 YAG:Tm spectrum and blackbody emission.

ing. The energy can be transferred between activators. Dexter energy transfer and Förster energy transfer are different mechanisms, but both produce the same end result. In our data, we cannot distinguish which mechanism is occurring, but we can account for energy transfer in our model for luminescence lifetime. If two activators are within a short distance, usually less than 10 Angstroms [58], and thus their electron wavefunctions overlap, the energy absorbed can move from one to the other in the form of charge. Dexter energy transfer is short-range, a Coulombic interaction that depends on the Wigner-Seitz radius. If the transfer distances is greater than 10 Angstroms and is thus a long-range transfer, FRET (Förster or Fluorescence Resonant Energy Transfer) is considered the mechanism of energy transfer. The FRET efficiency, or the quantum yield of the energy transfer is given by

$$E = \frac{1}{1+(\frac{r}{R_0})^6} \tag{2.3}$$

where E is the FRET efficiency, r is the distance between donor and acceptor, and R_0 is the distance between two dipoles when the transfer efficiency is 50%. R_0 can be calculated by

$$R_0^6 = \frac{9000 Q_0 (\ln 10) \kappa^2 J}{128 \pi^5 n^4 N_A} \tag{2.4}$$

where Q_0 is the fluorescence quantum yield of the donor, κ^2 is the dipole orientation factor, n is the refractive index, N_A is Avogadro's number, and J is the spectral overlap integral given by

$$J = \int f_D(\lambda) \varepsilon_A(\lambda) \lambda^4 d\lambda \tag{2.5}$$

where f_D is the normalized donor emission, and ε_A is the acceptor molar extinction coefficient. FRET can occur when there is an overlap in the absorption spectrum of one activator and the emission spectrum of another. This is an energy transfer that occurs without the movement of charge. The probability of energy transfer, direct emission, and direct quenching depends on the distances between two activators and between activators and quenching sites. The Wigner-Seitz radius for YBO_3:Ce^{3+} (shown in Figure 2.6) can be calculated using the unit cell parameters $a = 11.3138(3)$ Å, $b = 6.5403(2)$ Å, $c = 9.5499(2)$ Å, and $\beta = 112.902(1)^\circ$. as follows

$$d = 2 \left(\frac{3}{4 \pi x_a} \right)^{1/3} \tag{2.6}$$

where x_a is the concentration of 3+ sites being occupied by an activator, that is $x_a =$ mol%(12atoms per unit cell)$/(V_{UC})$. The volume of the cell is 650 Å^3. The Wigner-Seitz radius is about 10 Å at 10 mol% activator concentration. The radius is greater than 10 Å for activator concentrations below 10 mol% suggesting that the FRET transfer mechanism dominates.

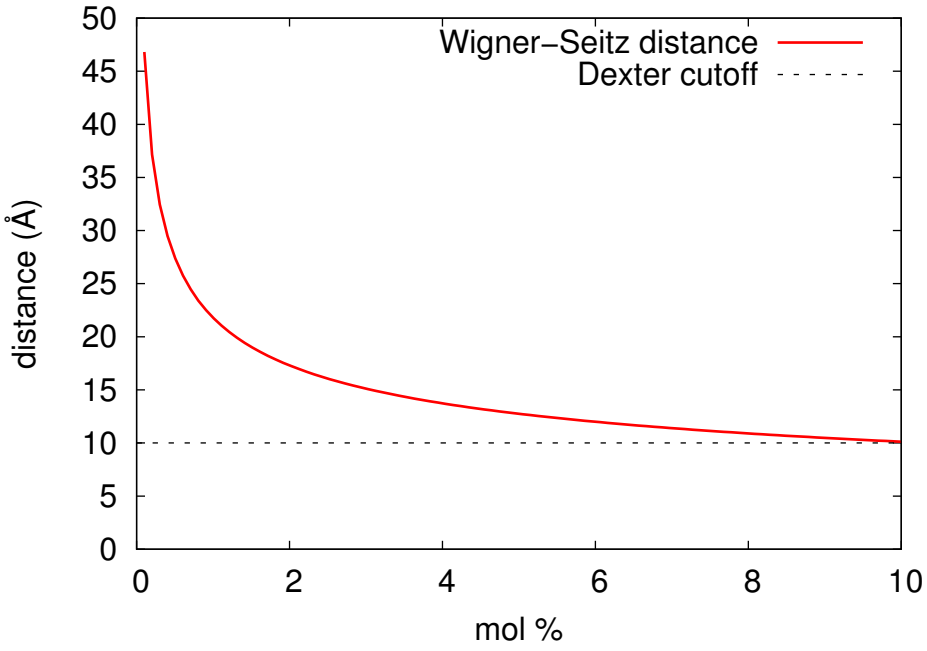

Figure 2.6 Estimation of the Wigner-Seitz radius for $YBO_3:Ce^{3+}$.

CHAPTER III

METHODS

3.1 Fabrication of $YBO_3:Ce^{3+}$

The chemicals used in the combustion synthesis of $YBO_3:Ce^{3+}$ were $NH_4B_5O_8$ (Sigma Aldrich, $\geq 99.5\%$), $Y(NO_3)_3 \cdot 6\,H_2O$ (Sigma Aldrich, 99.9%), glycine ($C_2H_5O_2N$, Sigma Aldrich Reagent Plus, $> 99\%$), NH_4NO_3 (Macron Chemicals, ACS Grade), $Ce(NO_3)_3 \cdot 6\,H_2O$ (Sigma Aldrich, 99.5%), and $Eu(NO_3)_3 \cdot 6\,H_2O$ (Pfaltz and Bauer, Inc., 99.9%). The resistivity of the deionized water used in these syntheses was $12.5\,M\Omega\,cm^{-1}$ or greater. To perform the synthesis, the reagents were added in stoichiometric ratio $Y(NO_3)_3 + 0.2\,NH_4B_5O_8 + 1.6\,C_2H_5O_2N \longrightarrow YBO_3 + 2.4\,N_2 + 3.2\,CO_2 + 4.4\,H_2O$; 0.006 moles of YBO_3 were made in each case. The reagents were weighed on a balance then added to a 50 mL alumina crucible. A 0.148 M $Ce(NO_3)_3 \cdot 6\,H_2O$ or 0.104 M $Eu(NO_3)_3 \cdot 6\,H_2O$ solution was used to add the dopant via an adjustable micro-pipettor. Because $NH_4B_5O_8$ lacks an oxidizer, a 1:1 ratio of NH_4NO_3 to every boron atom was added to provide oxidizer. The additional oxidizer was then balanced via $4.5\,NH_4NO_3 + C_2H_5O_2N \longrightarrow 5\,N_2 + 2\,CO_2 + 11.5\,H_2O$ with glycine to provide a balanced fuel:oxidizer ratio. The reactants were diluted in 2 mL of water. The crucible was placed on an 80°C hot plate and continuously stirred with a PTFE coated stir bar for 15 min. The stir bar was removed and the crucible was placed in a 600°C vented muffle furnace. Combustion took place within 3 min of being placed in the furnace. The material was then given a 2-hour heat treatment at 1000°C to burn off remaining carbonaceous residues.

Figure 3.1 Combustion synthesis.

3.2 Powder Sample Mounting

There were many constraints to consider when designing a way to hold the sample (in this case powder) for experiments. For the irradiation experiments, we chose to use the unadulterated powder–no binders, solutions, or shape processing. Binders can interfere with the photoluminescence, as demonstrated by Weeden-Wright and Gollub [59]. Solutions are not practical in vacuum environments where radiation and other characterization is required. Because the irradiation may not penetrate the entire sample and because the beam coverage is not uniform, we must ensure that the exposed powder is the same powder that is also examined by spectroscopy and decay.

The samples are tested under ionizing radiation (x-rays) so the material must be conductive to prevent charge buildup. The samples are also placed under vacuum in the pelletron (protons), tilted 90° to be irradiated (pelletron), and moved between the end station chamber and the photoluminescence/decay setup repeatedly. We tried using an epoxy and glue (separately) on a thin sheet of aluminum. From this we learned that superglue has an emission peak [59]. While the photoluminescence emission intensity of the LZO:Eu^{3+} did not significantly change due to the radiation exposure to 1 MeV protons, having a secondary luminescent material (the cyanoacrylate) was useful as a reference for the compar-

ison of degradation of the emission intensity. Although the effect was interesting, we want to see changes to just the phosphor rather than the phosphor and binder mix.

Another constraint to our sample holder is how to make sure the excitation light and radiation hit the same exact spot. Our photoluminescence/decay setup uses fiber with a 600 μm diameter, so the light coming out of the cable is about 2 or 2.5 mm when put close to the sample. Sometimes the emission is very weak, so the closer the fiber is to the sample, the more light gets back into the fiber and received by the spectrometer. Thus, the area where the photoluminescence/decay is measured is quite small. The beam size from the pelletron can be adjusted. We want the beam size to be small because there is less energy fluctuation and the experiments are faster. But the beam's spot size should be slightly larger than the sample size so that the deposited energy is uniform across the sample.

SRIM calculations were made to determine the penetration depth of alpha particles and proton particles through YBO_3. 3.4 MeV alpha particles penetrate 28 μm and 1 MeV protons penetrate 28 μm. This depth is important because we want to irradiate the entire sample, not just the top layer. The photoluminescence may query a different depth than the irradiation.

Our final design is a 10 mm $\times$ 10 mm $\times$ 2 mm aluminum square with a 2 mm diameter indentation ($0.5 - 1$ mm deep) in the center. We take a small amount of powder from the vial and press it into the indentation with a flat spatula. We repeat this until the indentation is compact and filled. To create an even surface, we use a blade to scrape away excess powder.

3.3 Photoluminescence

Photoluminescence measurements were taken with an Avantes 2048 USB2 spectrometer. The excitation was provided by a xenon light source that goes through a Newport Oriel 130 1/8 monochromator. The monochromator allows selection of the excitation wave-

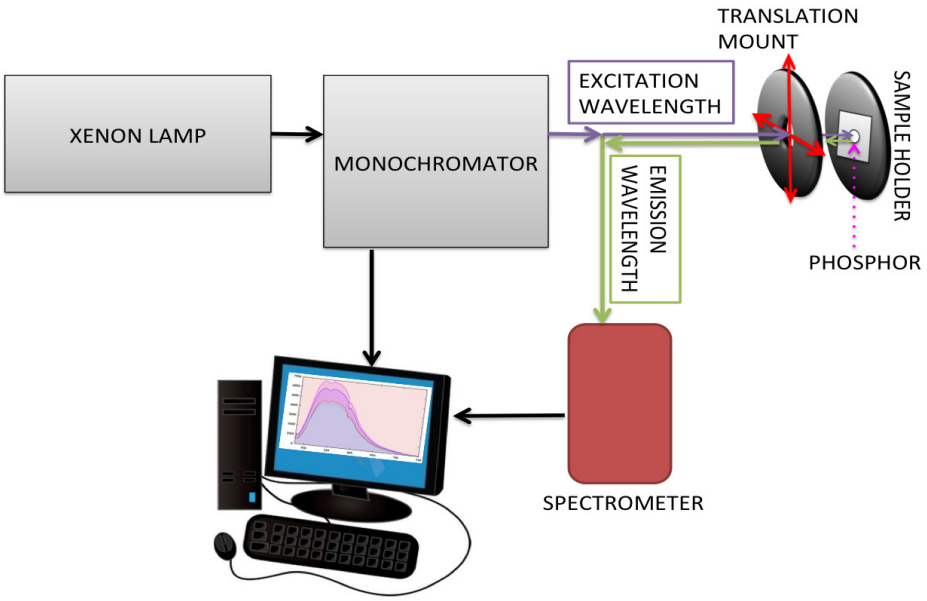

Figure 3.2 Schematic of photoluminescence setup.

length. The light passes through one leg of a bifurcated fiber optic cable to a translation mount that can be adjusted to align the light with the sample. This leg of the cable both sends out the excited light and receives the emitted light from the phosphor. The third leg of the cable takes the emitted light to the spectrometer where it is translated into a spectrum. The sample holder is placed in a custom 3D rapid-prototype printed fixture that sits stationary in a filter adapter as seen in Figure 3.3 The fiber cable connects to an SMA adapter that is screwed into a small x-y translation stage. By using the translation stage and the Avantes Avasoft software set with a low integration time, we can identify the position at which the emission is greatest and the excitation/reflected peak is minimized (this happens simultaneously). This centering on the sample ensures that same exact spot is queried before and after irradiation. In addition, a dark spectrum is saved and subtracted from each measurement right before data collection to remove stray or background light from contaminating the signal.

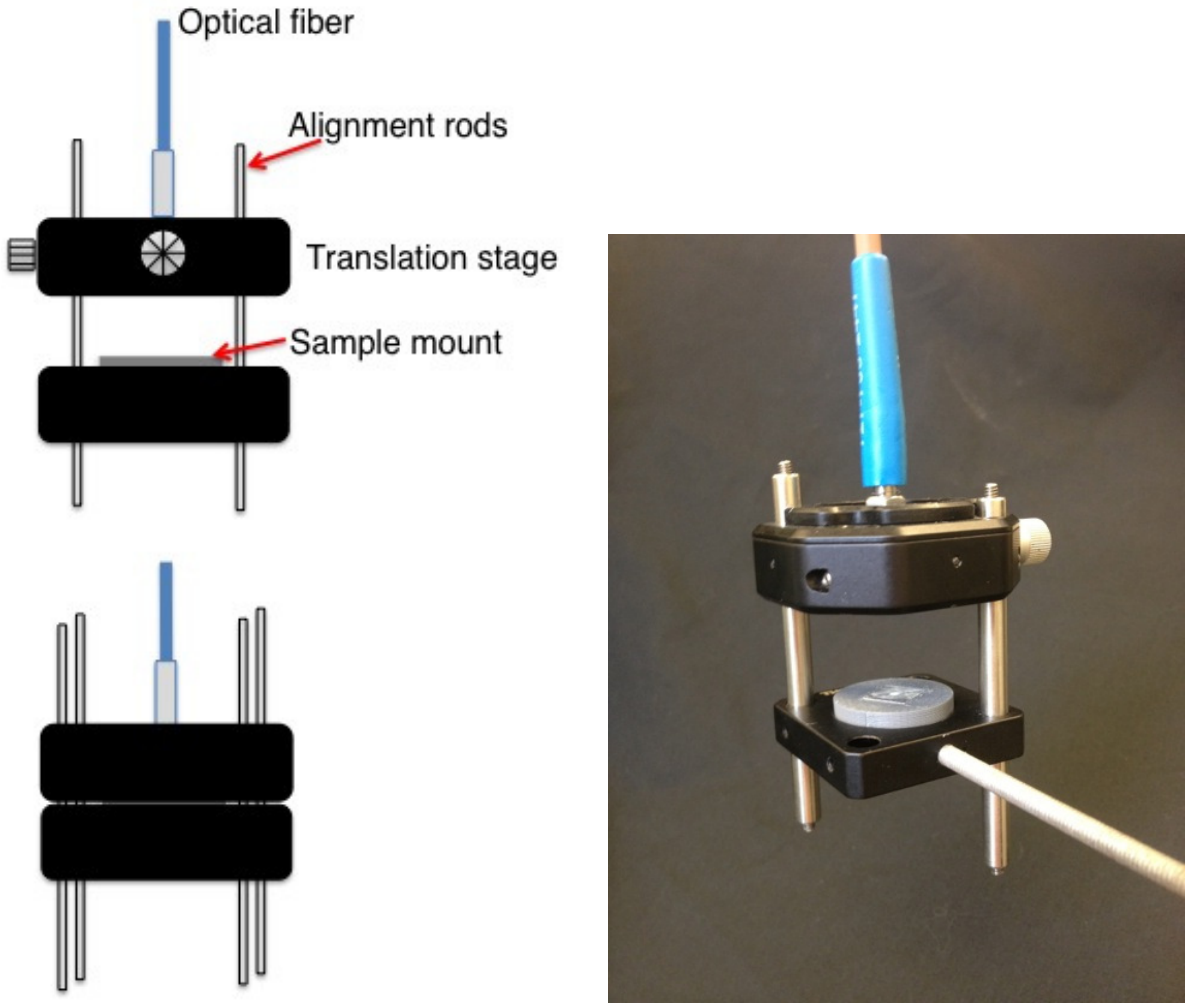

(a) (b)

Figure 3.3 The sample is mounted and placed into the plastic holder under the fiber cable. The two black pieces can be pushed closed to create a dark environment for photoluminescence. Figure (a) shows the sample holder open (upper) and closed (lower).

Because the material is a powder, we assume that all properties are dominated by scattering and are, therefore, diffuse [60]. Consequently, the values are effective properties of the powder, not actual material properties for pure crystalline materials of the same constituents. We have also assumed that the excitation efficiency α and reflectivity ρ are independent of the frequency of the excitation light and emission light. Strictly this approximation is not valid; however, we can not distinguish between these properties from the measurements we have made, so identifying separate absorptivities and reflectivities is unnecessary.

Even if the properties are considered diffuse, the geometry will change the overall ratio of collected emission to collected reflected light. This effect does not appear in the formulation but is not important as long as the geometry of the fiber relative to the sample is maintained for each measurement. For example, if the fiber is not aligned with the sample, the excitation light could reflect off the aluminum sample holder instead of the sample itself. Therefore, the sample holder was placed in a translation stage and the sample moved until the reflected light was minimized. At this position, most if not all of the excitation light falls on the sample whose reflectivity is less than that of the aluminum holder. This position also corresponds to where the emission is maximized because the sample was being exposed to the greatest amount of excitation light in this configuration.

Because relative intensity measurements are hard to measure consistently, we normalized our data. We normalize the entire spectrum to accommodate any variations or uncertainties in the setup such as fluctuations from the lamp, slit widths from the monochromator, losses from transmission through filters/fibers/connections, phosphor intensity, etc. We fits Gaussian curves to each of the peaks in the spectrum–one curve for the excitation/reflection and one curve for each transition in the emission (which sometimes overlap, as in YBO_3:Ce^{3+}). From the fit we find the integral of the excitation/reflection peak. The entire spectrum is divided by this value (integral normalization). By taking the integral of the excitation/reflection peak, we remove the dependence of the output on the monochro-

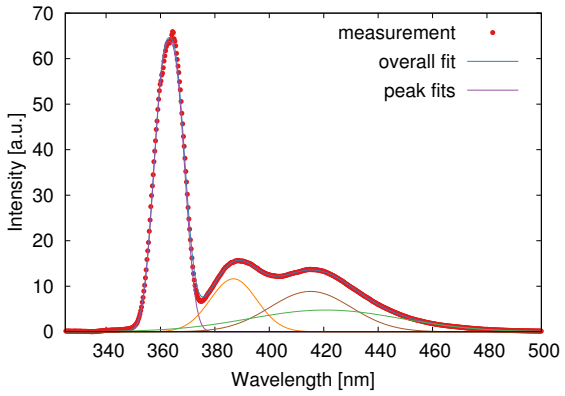

Figure 3.4 An example of the Gaussian curves fit to the photoluminescence of YBO_3:Ce^{3+}.

mator and excitation strength that may affect the overall intensity of the spectrum.

The excitation spectrum, Figure 3.5, indicates the wavelengths (energy) where the material absorbs the most light. The monochromator sweeps from 300 nm to 800 nm while the spectrometer measures the emission at each wavelength. The wavelengths that produce strong emissions are the excitation wavelengths.

Emission spectra are measured by selecting the excitation wavelength(s) with the monochromator (or a laser in the case of lifetime measurements) and adjusting the integration time and number of averages to acquire an accurate representation of the emission.

The emission spectra can provide valuable information about the material. The emission peaks indicate the energy level transitions from the excited state down to the ground state. Some peaks can be electronic dipole transitions and others can be magnetic dipole transitions. In addition, the number of peaks per transition can indicate crystal field splitting. The symmetry of the environment of the luminescent center has an effect on the number of peaks. Europium, for example, has a peak at 612 nm that is the $5\,d \longrightarrow 4\,f(^7F_{5/2})$ transition, but it can split into as many as four peaks near 612 nm depending on its symmetry in the lattice.

Repeatability studies were done to provide an error range of photoluminescence

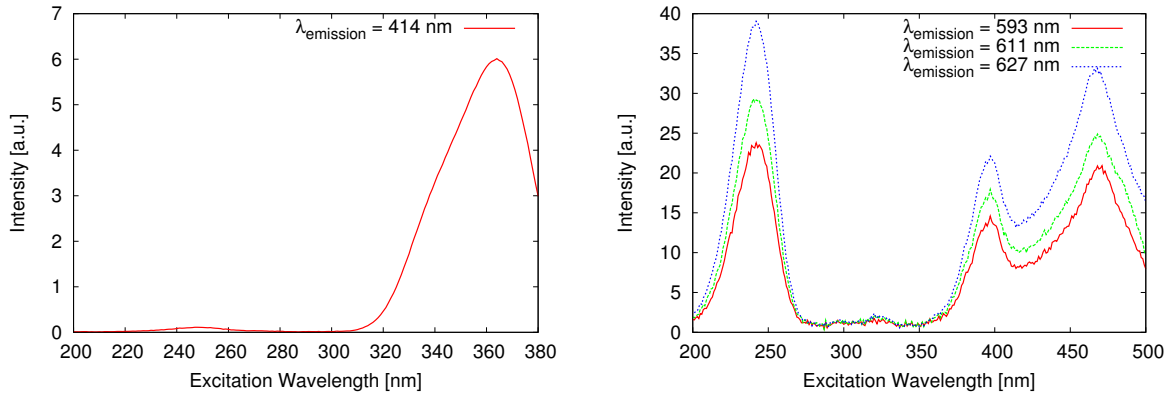

(a) (b)

Figure 3.5 Excitation spectrum of (a) YBO_3:Ce^{3+} and (b) YBO_3:Eu^{3+}.

emission measurements. Five samples of YAG:Ce^{3+} from the same batch were packed into holders. The process of centering, removing the dark background, and normalization were done on each sample. In addition, one sample was tested five times. The results of this test can be seen in Figure 3.6.

Because absolute intensity measurements are difficult to measure consistently and across samples, we normalized our data to the integral of the reflected excitation peak as measured by the spectrometer. By normalizing in this way, we remove any variation in the excitation light due to lamp fluctuations, varying slit width on the spectrometer, or intensity variations inherent to the lamp for different wavelengths.

The normalized measurement can be represented as a combination of material properties showing that the measurement is indeed independent of the intensity of the excitation beam. Therefore, measurements made before and after irradiation can be compared, and any change will indicate a change in the material properties due to radiation, not changes in the photoluminescence measurement technique. Figure 3.7 shows how the light interacts with our sample and provides a pictorial representation of the normalized measurement. The spectral intensity of the emission $I_{\lambda m}$ and the spectral intensity of the reflected light $I_{\lambda r}$ are the magnitude of the corresponding peaks from the spectral measurement. We can

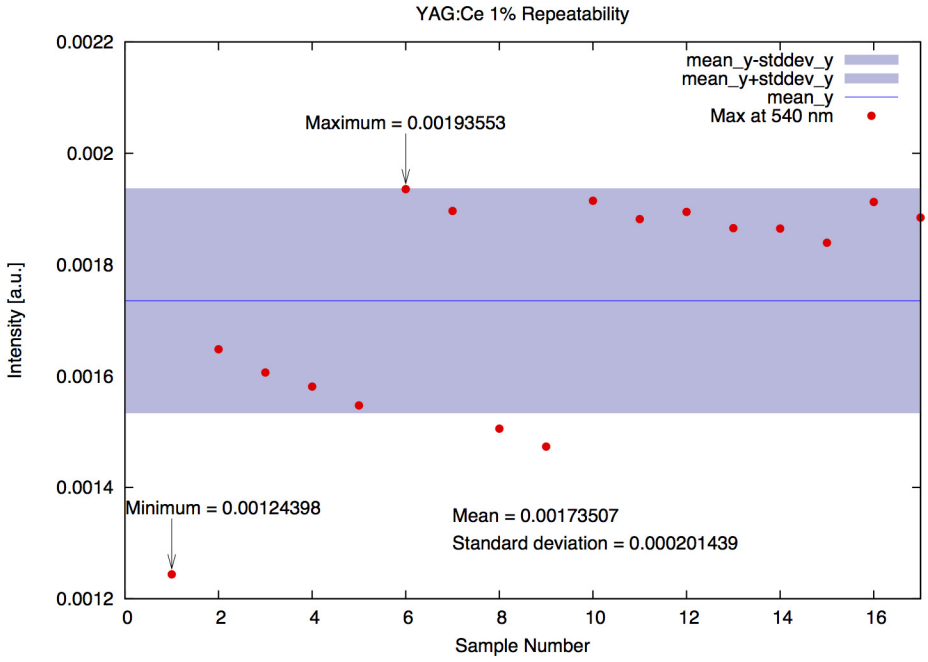

Figure 3.6 Repeatability tests of YAG:Ce^{3+}.

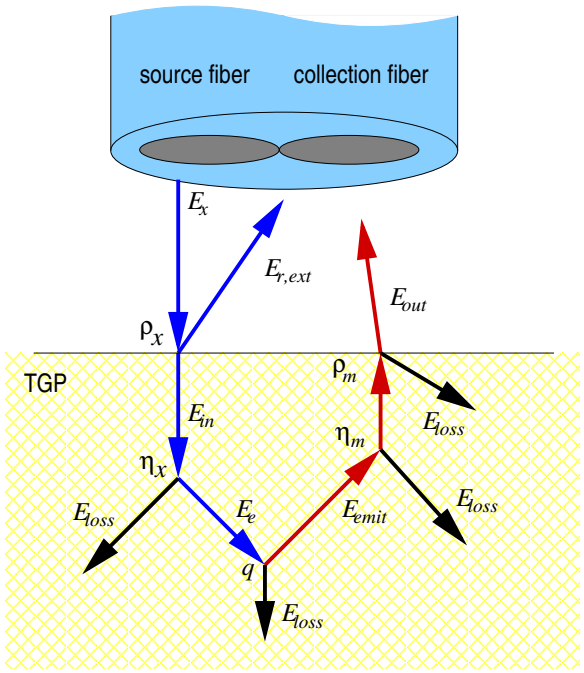

Figure 3.7 The excitation light that illuminates the sample emanates from the end of a bifurcated fiber optic. The other fiber, collects reflected and emitted light.

write the emission and reflected intensities as a function of the unknown incident excitation and effective material properties such that

$$I_{\lambda r} = \rho I_{\lambda x} \quad \text{and,} \tag{3.1}$$

$$I_{\lambda m} = (1-\alpha)^2(1-\rho)^2 q I_{\lambda x}. \tag{3.2}$$

where ρ is the reflectivity of the sample, q is the quantum yield, and α is the loss due to absorption by the host lattice. Refer to Figure 3.7 for the relationship between the intensities and the properties used in this formulation. The ratio of emitted intensity to reflected intensity (what we call overall yield) is given as

$$Y_\lambda = \frac{I_{\lambda m}}{I_{\lambda r}} = \frac{(1-\alpha)^2 q (1-\rho)^2}{\rho}, \tag{3.3}$$

We can also define total quantities which are integrated over the Gaussian fit of a peak. For example,

$$I_x = I_{\lambda x} \int_0^\infty \exp\left[-\frac{(\lambda-\mu_x)^2}{2\sigma_x^2}\right] d\lambda = I_{\lambda x}\sqrt{2\pi}\sigma_x, \tag{3.4}$$

where σ_x is the standard deviation of the peak, and μ_x is the center of the peak. In the gray approximation, the reflected and excitation center will be the same, and the reflected and excitation standard deviation will be the same. Therefore, the total overall yield can also be expressed in terms of parameters gleaned from the spectral measurements and the same effective properties used in Equation 3.3.

$$Y = \frac{I_m}{I_r} = \frac{\sigma_m}{\sigma_r}\frac{(1-\alpha)^2 q(1-\rho)^2}{\rho} \tag{3.5}$$

The foregoing formulation shows that any changes in the normalized spectrum due to irradiation suggest that the effective material properties were altered by the incident particles. On a simplistic level, we can understand how particle radiation might create defects as atoms in the sample are bombarded. The defected sample then might exhibit more scattering, which could show up in our measurements as a increased absorption coefficient α. Similarly, more defects would also increase quenching and reduce the quantum yield q. We can not distinguish between these effects, and the sample may actually see a combination of effects, but we are ultimately looking for a change in the spectrum after irradiation.

3.4 Decay

Since the fiber is positioned ideally above the sample, we can easily move the other ends of the fiber to measure the lifetime. The end connected to the monochromator can be switched to connect to a laser, and the other leg that is connected to the spectrometer to a PMT.

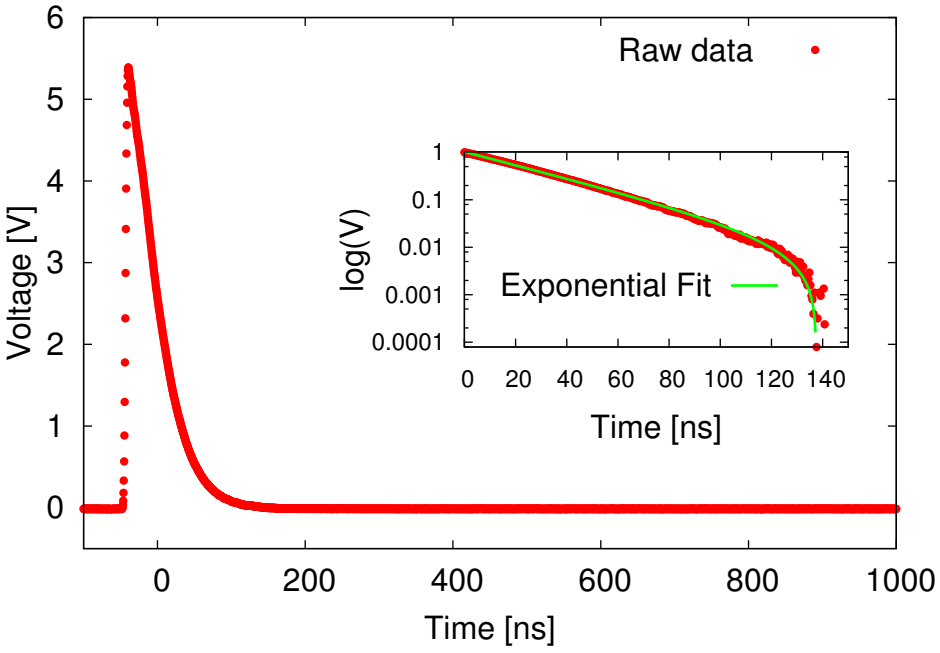

Figure 3.8 Example raw decay with example fit (inset).

To measure the luminescence lifetime of YBO_3:Ce^{3+}, a switched 337 nm nitrogen laser (Newport NL100) at a repetition rate of approximately 30 Hz with a 170 μJ pulse energy excites the sample. A photomultiplier tube (PMT Hamamatsu model H10721-20) connected to an oscilloscope (Tektronix DPO3034) collects the emission. The emission passes through a 360 nm long-pass filter, a 415 nm band pass filter, and an ND filter (two layers of weigh-paper) to reduce the saturation of the laser light within the signal. A 50 Ω termination was used to record fast transients. A typical trace of the raw data that originates from the oscilloscope is shown in Figure 3.8 along with an example fit of the data used to determine the decay time. The slope of the linear portion in the log plot is the decay time.

To measure the lifetime of europium-doped samples, a 200 mW Coherent OBIS 405 nm LX laser is connected to a Tektronix AFG3021C function generator.

3.5 XRD

Materials were characterized by x-ray diffraction (XRD) to verify the crystal structure and integrity of the as-fabricated powder. XRD data were collected on un-irradiated bulk samples because our sample size for radiation tests were too small to measure XRD after irradiation. Measurements were taken using a Scintag X-1 powder x-ray diffractometer with CuK$_\alpha$ radiation (1.5418 Å). Scans were run at 45 kV and 40 mA. Although the crystal structure of yttrium borate has been highly debated [29, 61–63], the XRD characterization (Figure 3.9) affirms that our product's structure matches the JCPDS reference for yttrium borate. XRD can provide indications about whether the sample is entirely yttrium borate, or if other yttrium-oxygen-boron materials are present in our product. Although we cannot determine the purity from XRD alone, we can determine whether the crystal structure is changed by the dopant. In this case, yttrium borate maintained its crystal structure even when doped with cerium or europium. See Figure 3.9.

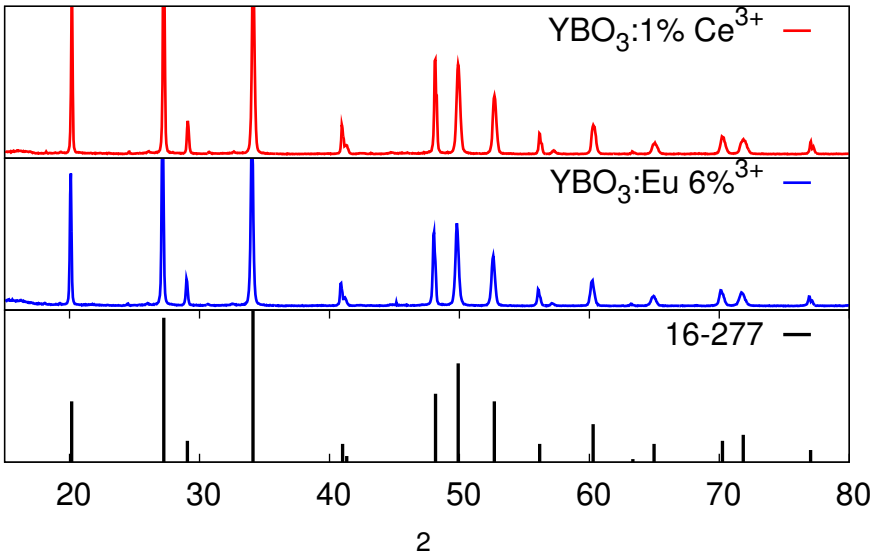

Figure 3.9 XRD spectra of YBO_3:Ce^{3+} and YBO_3:Eu^{3+} with JCPDS reference.

3.6 Irradiations

We hypothesize that non-ionizing radiation at an appropriate fluence can permanently damage a phosphor. Photoluminescence and lifetime of the phosphor provide information about whether or not the material has been exposed to damaging radiation. This is the first step to using phosphors as a tool to detect radiation. By exposing the material to a suite of radiation types, fluences, and energies, we can begin to distinguish the effects of radiation.

3.6.1 X-Rays

The phosphors were exposed in an ARACOR 4100 tungsten X-ray source with a beam size of approximately 3 cm in diameter. The X-rays at 1 Mrad fluence and a dose rate of 31.5 Krad SiO/min did not change the photoluminescence spectra in either YBO_3:1%Ce^{3+} nor in YBO_3:6%Eu^{3+}. This result is expected because x-ray radiation is ionizing, therefore the probability of displacement damage is unlikely.

3.6.2 Alphas

For alpha irradiation of YAG:1%Ce^{3+} and LZO:5%Eu^{3+} using ^{241}Am, four samples were laid in a square (2×2) and the 12 mm $\times$ 12 mm source was put directly on top. The ^{241}Am has an activity of 8.8 μCi and energy of approximately 5.5 MeV. The alpha irradiations were done in air, not in vacuum, which means the particles have less energy (3.4 MeV compared to 5.5 MeV). YAG:1%Ce^{3+} and LZO:5%Eu^{3+} were exposed for 10 minutes, 30 minutes, and 1 hour, which corresponds to a fluence of 6×10^5, 1.8×10^6 and 3.6×10^6 particles/mm^2 respectively. Results are shown in Figure 4.2.

Alpha irradiation of YBO_3:1%Ce^{3+} and YBO_3:6%Eu^{3+} were done also in the pelletron using helium gas. Photoluminescence emission was measured after 1, 5, 29, and 101 hours, which corresponds to 8.14×10^8, 4.07×10^9, 2.36×10^{10}, and 8.22×10^{10} alphas/cm^2.

The results, which are provided in Figure 4.6 (a), show an insignificant (within the noise) decrease in the overall intensity of the spectrum for both materials.

Alpha irradiation of EuD_4TEA using ^{241}Am and ^{210}Po were performed with two methods. The first method used a cap of powder sample with the source chip resting over the top. The second method used a thin-film (EuD_4TEA dropcasted onto microscope slide) and the source chip held just above the sample.

3.6.3 Protons

The first few proton irradiation experiments (on YAG and LZO) were performed in the Vanderbilt VINSE Van de Graaff and the subsequent experiments carried out in the pelletron accelerator. H^+ gas was used to produce 1 MeV protons.

The accelerator proton beam was focused to 4 mm and centered on the sample. The beam profile from previous experiments is assumed to be Gaussian where the diameter is approximately the FWHM of the beam. Consequently, the region of the beam incident upon the sample was reasonably uniform, although the edges (at 1 mm from the center) received 15% less intensity than the center. We are required to move the aluminum holder between the spectroscopy stage and the accelerator end station between each irradiation, so we can't ensure that exactly the same spot is targeted after each step. Therefore, the uniformity of irradiation is important to minimize the uncertainty of the exposure across the sample, and the wide beam allows consistent measurements between steps.

3.6.4 Neutrons

Neutron irradiation tests were performed at the Ohio State University Research Reactor (OSURR). The fuel at OSURR is 19.5% enriched U_3Si_2. For our tests, we used the pneumatic transfer (rabbit) facility. The neutron energies in the rabbit facility vary from thermal energies (0.0253 eV) up to $18-20$ MeV. For the rabbit, 68% of the neu-

trons are less than 1 eV and 18% are epithermal (between 1 eV and 0.5 MeV). The remaining 14% are fast (> 0.5 MeV). The neutron flux in the rabbit over all energies is $2.4 \times 10^{12}\,\mathrm{n/cm^2/sec}$ at a reactor power of 450 kW. When operated at lower powers, the neutron flux is scaled appropriately.

CHAPTER IV

RESULTS

4.1 Screening with X-rays

The first material we fabricated and tested was yttrium aluminum garnet doped with cerium (YAG:Ce^{3+}). We started with YAG:Ce^{3+} because there is already a great deal of information in the literature about it, and it is easy to make. In addition, our lab has previous experience with fabricating and measuring the photoluminescence and decay of YAG:Ce^{3+}.

Our first radiation experiment exposed YAG:1%Ce^{3+} to x-rays using an ARACOR 4100 tungsten source. X-rays are ionizing radiation, so we did not expect to see any change in the photoluminescence. We irradiated samples of material with 10 keV x-rays at 100 krad, 500 krad, and 1 Mrad and took a photoluminescence spectrum after each dose. As shown in Figure 4.1, there were no discernible changes in the spectra after irradiations.

4.2 Alphas with ^{241}Am and Protons in Van de Graaff

The second material tested was lanthanum zirconate doped with europium (LZO:4%Eu^{3+}). We decided to try europium as the dopant rather than cerium because europium has a narrow line emission spectrum. There are more transitions (and peaks), the peaks are sharper, and they peaks do not overlap the way cerium does. Unlike cerium, whose transition levels depend on the presence of the lattice, europium has several intrinsic transitions that are largely independent of the lattice. However, the lattice can cause splitting of europium levels. We thought perhaps some peaks could be more sensitive to the radiation than others. For this test, we glued phosphor powder onto an aluminum square 1.5 cm $\times$ 1.5 cm using generic cyanoacrylate (Gorilla super-glue). We exposed LZO:4%Eu^{3+} to x-rays to ver-

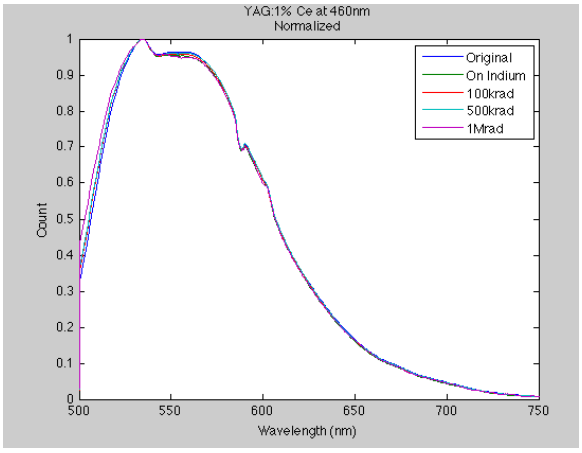

(a)

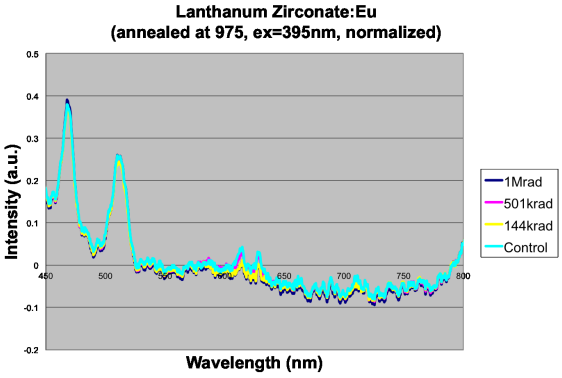

(b)

Figure 4.1 Photoluminescence emission results from x-ray irradiations of (a) YAG:1%Ce^{3+} and (b) LZO:4%Eu^{3+}.

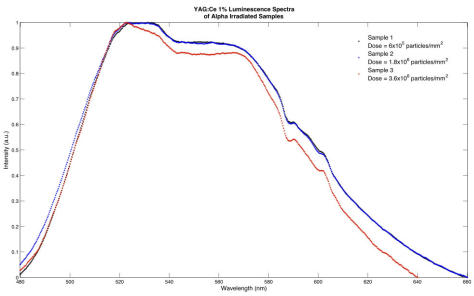

Figure 4.2 Photoluminescence emission results from alpha irradiations of YAG:1%Ce^{3+}.

ify our method of measuring photoluminescence and decay between irradiations and from sample to sample.

Then we did proton irradiation in the VINSE Van de Graaff. The intensity of the photoluminescence emission degraded after each irradiation, but an emission peak, which turned out to be from the glue, increased. Unfortunately, after removing the glue component of the experiment, we were unable to recreate the data that showed degradation of the LZO:4%Eu^{3+} emission [64]. These were not step-stress experiments, but individual samples each irradiated to a different dose.

In addition to the pre-irradiation and post-irradiation photoluminescence measurements, we took scintillation data. Although the focus of this project is not about scintillation, we can still learn about the material by examining the cathodoluminscence. An SLR camera was positioned to view through the Van de Graaff porthole and the camera parameters (aperture, exposure time, focus, etc.) were kept constant throughout the experiment. Pictures were taken at intervals during the radiation. One pixel from each shot was broken down into red, blue, and green channels with their respective intensities, as seen in Figure 4.3. Europium in LZO:Eu^{3+} emits in the red region, so it was not too surprising that the blue and green components did not change over time. The red channel, however, decreased with time. This decrease can be modeled with a standard exponential, as seen in Figure 4.3. We expect standard exponential behavior because the degradation is cumulative as time passes and therefore, as quenching occurs there are fewer opportunities for luminescence emission.

$$I = I_0 e^{-t/\tau} + I_{off} \tag{4.1}$$

where $I_0 = 150$, $\tau = 47\,\text{min}$, and $I_{off} = 130$.

Upon removal from the end station, we noticed the powder had turned from white to yellowish gray, as seen in Figure 4.4. The area of color change was approximately equal to the proton beam raster area suggesting that the color change was a result of the radiation.

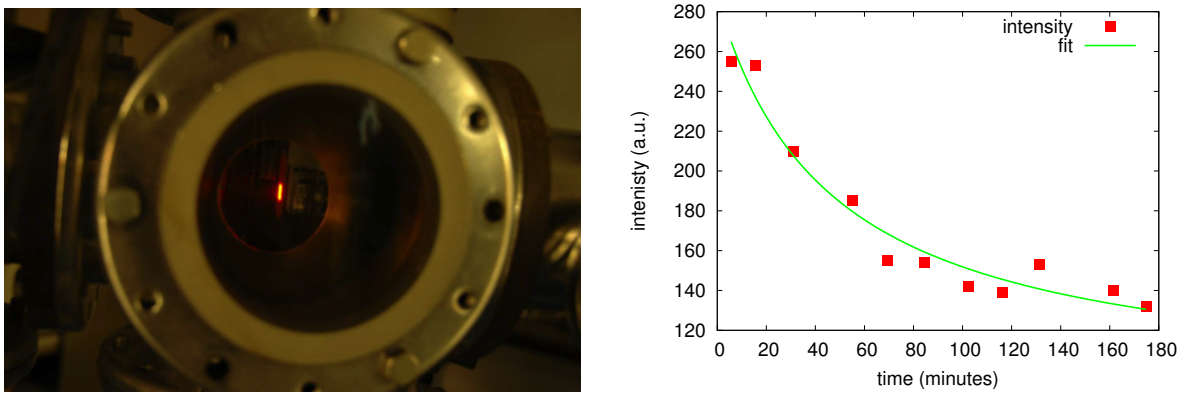

(a) (b)

Figure 4.3 (a) Cathodoluminscence as seen by looking through porthole at target during irradiation in VINSE Van de Graaff. (b) Cathodoluminscence of LZO:4%Eu^{3+} showing degradation of red channel.

We can not rule out the possibility that there were contaminants in the end station that interacted with the radiation or the sample and resulted in the color change (i.e. carbon buildup).

The third material we fabricated and tested was yttrium borate (YBO_3). We tried doping it with cerium, europium, and a combination of cerium and europium. Our first experiments were with YBO_3:1%Ce^{3+} and YBO_3:6%Eu^{3+}. We used 1% Ce^{3+} because that amount was used in YAG, and 6% Eu^{3+} because preliminary quenching concentration experiments (via REU student Justin Colar) and the literature suggested 6%. After some of the initial experiments (October 2012), we performed concentration studies and determined that 1% Ce^{3+} or 20% Eu^{3+} in YBO_3 is the ideal amount for measuring the most intense emission. Co-doped material was explored, but as the concentration of cerium was increased, the europium signal quenched, so these samples were not irradiated. YBO_3:1%Ce^{3+} and YBO_3:6%Eu^{3+} were exposed to alpha and proton radiation. Multiple samples of each powder (same batch) were measured for photoluminescence before and after each step of irradiation.

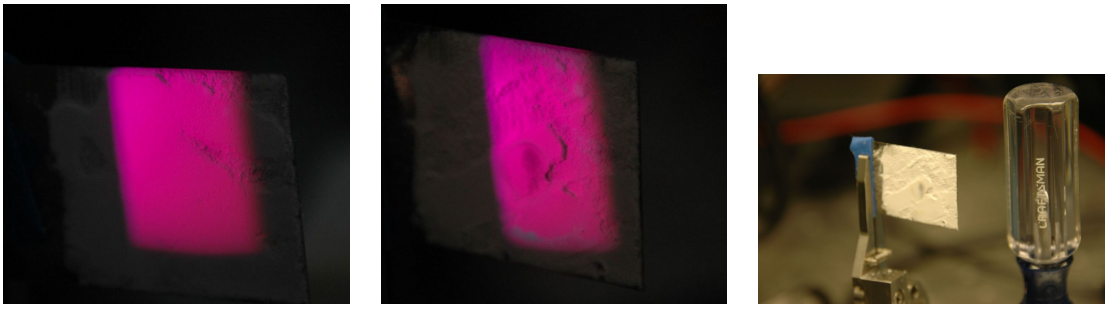

(a) (b) (c)

Figure 4.4 Luminescence from LZO:Eu^{3+} (a) before proton irradiation and (b) after proton irradiation, which shows a dark area where the beam hit the sample. (c) LZO:Eu^{3+} in incandescent light after proton irradiation also reveals the dark area where the beam hit the sample.

The results, which are provided in Figure 4.5(a), show an insignificant (within the noise) decrease in the overall intensity of the spectrum for both materials, YBO_3:1%Ce^{3+} and YBO_3:6%Eu^{3+}. Figure 4.6 (b) shows the intensity of the photoluminescence spectra does not appear to change with fluence. Although we expect some damage to present itself for particle radiation, the lack of change in the spectrum could be due to 1) an insufficient fluence to create enough damage to be visible, 2) an inappropriate alpha energy to interact with the crystal, 3) a poor choice of material that is relatively immune to alpha irradiation, or 4) low penetration of radiation into the material. However, the alphas could have produced damage that was undetectable by photoluminescence. Therefore, another possible explanation for lack of change in the photoluminescence is the small penetration depth of alpha particles in YBO_3. A SRIM [65] calculation indicates the penetration depth of 3.4 MeV He^{2+} particles in YBO_3:$Ce^{3+}$and YBO_3:Eu^{3+} to be 17.28 μm and 17.56 μm respectively. The depth of the light penetrating the sample is greater than the depth of the damage caused by the alphas, such that even if there is damage, it may not be visible because the luminescence from the un-damaged volume overwhelms changes in the damaged portion.

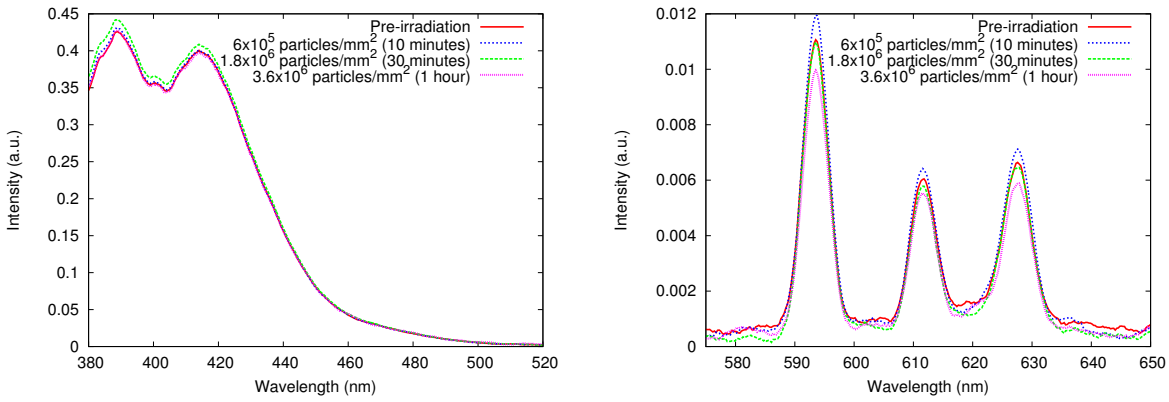

Figure 4.5 Photoluminescence emission results from alpha irradiations of (a) YBO_3:1%Ce^{3+} and (b) YBO_3:6%Eu^{3+}using ^{241}Am.

Table 4.1 TRIM calculations for approximate radiation damage in YBO_3:Ce^{3+} and YBO_3:Eu^{3+}.

Source	Vacancies/Ion	Fluence	# of Defects
H^+	7.5	1×10^{14} (min)	7.5×10^{14} (min)
H^{2+}	118	2.09×10^6 (max)	2.47×10^{10} (max)

SRIM calculations for 1 MeV H^+ particles in YBO_3:Ce^{3+} indicate a penetration of approximately 20.59 μm, and 20.87 μm for YBO_3:Eu^{3+}. Although the penetration is deeper for protons than with alphas, the distance is comparable. As will be seen in the subsequent section, a degradation of photoluminescence for proton irradiated material is evident. Therefore, we conclude that damage produced by the alphas should be detectable by the photoluminescence. Since we did not see significant change in the photoluminescence in the alpha irradiated material, we conclude that the material was not damaged enough for detection. Table 4.1 shows the number of vacancies estimates from TRIM calculations based on a the minimum fluence achievable for protons and the maximum fluence for alphas. One measurement of displacement damage provided by the TRIM tool is vacancies per ion which is 118 for 3.4 MeV alphas and 7.5 for 1 MeV protons in YBO_3. If we

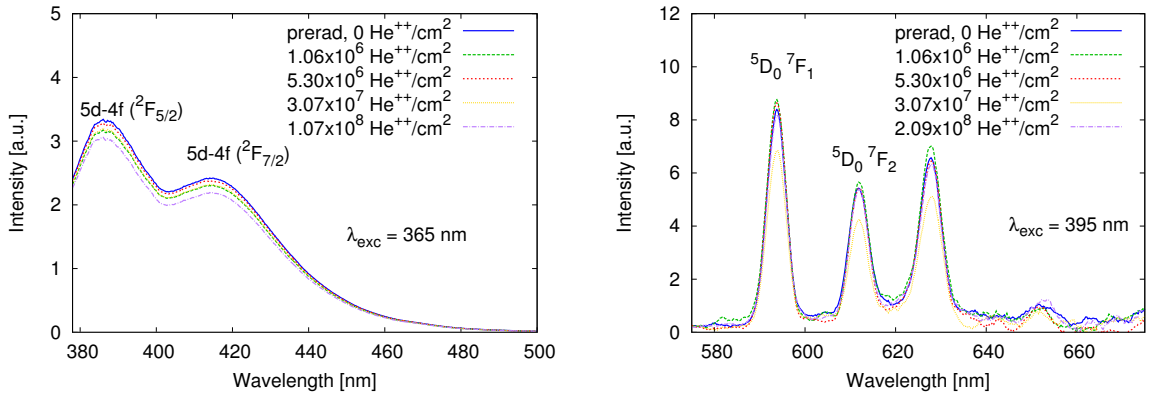

Figure 4.6 Photoluminescence emission results from alpha irradiations of (a) YBO_3:1%Ce^{3+} and (b) YBO_3:6%Eu^{3+} in the pelletron.

multiply the fluence with the vacancies per ions, we can get an idea of how much damage was caused by irradiation. Therefore, the most amount of damage we were able to achieve with alphas was 2.47×10^{10} vacancies compared to a minimum of 7.5×10^{14} vacancies with protons. We were unable to test the phosphors under proton irradiation at such low fluences, so a direct comparison cannot be made.

4.3 Alphas and Protons in Pelletron

All subsequent proton experiments were carried out using a newer pelletron accelerator. Three samples of each material were exposed to 1 MeV protons at 10^{14}, 5×10^{14}, 10^{15}, and $5 \times 10^{15}\,H^+/cm^2$. The overall intensity of the emission with increasing proton dose is apparent in both YBO_3:Ce^{3+} and YBO_3:Eu^{3+}. Decay was measured before and after each irradiation step as well. The lifetime of the irradiated sample increased initially and then decreased upon further irradiation, as seen in Figure 4.10. We expected the lifetime to decrease monotonically. This result is interesting because it suggests that the photoluminescence and the decay behave independently.

Assuming the material is damaged by the proton irradiation, the decrease in photo-

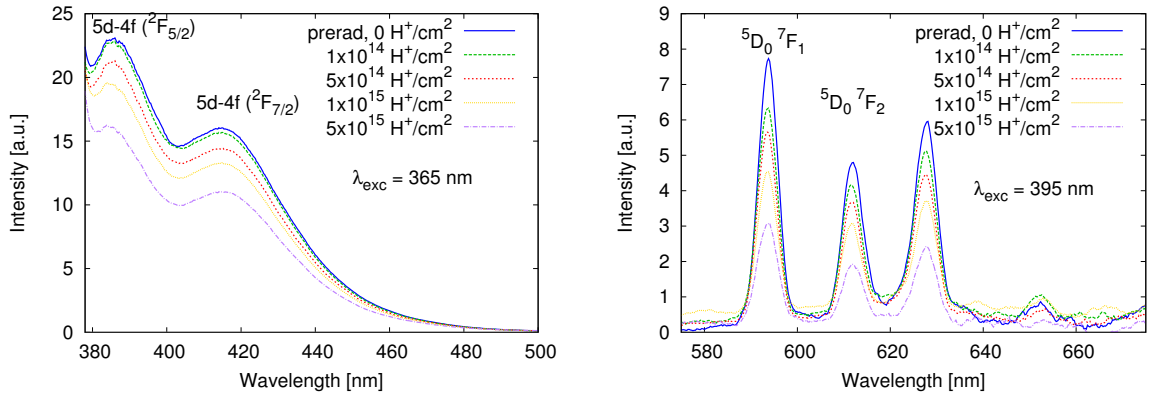

(a) (b)

Figure 4.7 Photoluminescence emission results from proton irradiation of (a) YBO_3:1%Ce^{3+} and (b) YBO_3:6%Eu^{3+}.

luminescence is probably the result of the increase in number of quenching sites created by the radiation-induced displacements.

Referring to equation 3.3, we can understand the decrease in yield as a decrease in q. Alternatively, the absorption of the material might increase with defects because the optical depth will decrease. In equation 3.3, this effect will show up as an increase in absorptivity. Both effects, which result in a decrease in yield, may be present in the material. However, we can not distinguish these effects using our measurements. A more detailed model and perhaps more detailed measurements are needed to resolve which effect dominates. Nevertheless, we can observe a strong dependence of the photoluminescence on the radiation dose.

The intensity of the emission of the first peak [5 d $\longrightarrow$ 4 f ($^2F_{5/2}$)] in the YBO_3:Ce^{3+} does not change significantly from the pre-irradiated dose to 1×10^{14} H^+ cm^{-2}. The subsequent intensity measurements for increasing dose all decrease monotonically. The intensity of the second peak [5 d $\longrightarrow$ 4 f ($^2F_{7/2}$)] also consistently decreases with increasing proton dose. These trends are shown in Figure 4.8.

The lines in Figure 4.8 are fits using the Birks and Black model (equation 2.1). The

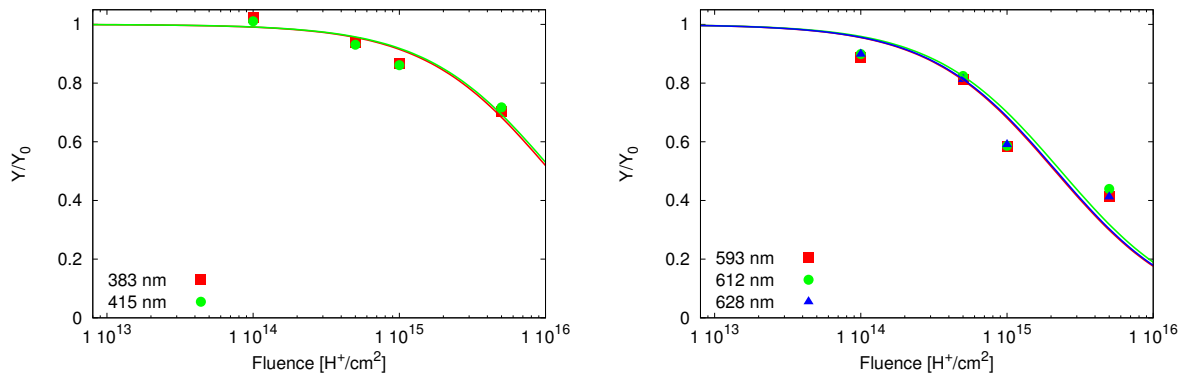

(a) (b)

Figure 4.8 Peak intensity for the transitions in (a) YBO_3:Ce^{3+} and (b) YBO_3:Eu^{3+}. The lines are fits using Birks and Black model.

adjustable parameters are the initial (un-irradiated) yield and the half-brightness dose. The half-brightness dose gives an idea of the sensitivity of the material to radiation exposure. In other words, the half-brightness dose can be used to compare materials and radiation environments. As shown in Figure 4.8, the data match the model well with the half-brightness dose calculated as $9.85 \times 10^{15}\,\mathrm{cm}^2$ for the $^2F_{5/2}$ and $9.24 \times 10^{15}\,\mathrm{cm}^2$ for the $^2F_{7/2}$. The values are within 6% of each other meaning that both peaks experience the same effect with dose. The europium-doped samples exhibit similar trends with the half-brightness dose for all peaks averaging $1.81 \times 10^{15} \pm 0.065 \times 10^{15}\,\mathrm{cm}^2$, which means that YBO_3:Eu^{3+} is more sensitive than YBO_3:Ce^{3+}. Both the cerium- and europium-doped samples are below their respective optimal concentration, where the maximum emission intensity is achieved. Other researchers have determined the optimal concentration of Ce^{3+}in YBO_3 to be around 0.5% [66, 67], although bulk YBO_3:Ce is commonly synthesized with 1% doping [68]. In addition, it has been found that the quenching concentration of europium in YBO_3 increases with decreasing particle size. Bulk YBO_3:Eu^{3+} is often made with only 5 or 10% dopant, but the optimal europium concentration is around 30% [31, 69]. Our material at 6% is almost certainly below the quenching concentration for YBO_3:Eu^{3+}. This is impor-

tant because the mechanism for quenching is different depending on the region. At doping levels above the optimal concentration, luminescent centers are close enough to initiate resonant transfer. Excited luminescent centers will transfer their energy to other luminescent centers via resonant transfer mechanisms at a rate faster than the emission. If the energy is transferred to a location near a defect center, that excitation is quenched instead of emitted. This is why the luminescence decreases at higher doping concentrations. At doping levels below the optimal concentration, the relationship between doping concentration and emission intensity is linear because transfer mechanisms are not possible in dilute concentrations. The quenching mechanism at low doping levels is dominated by defect center quenching.

In the radiation experiments we are adding defects that quench the luminescence through direct interaction of the defects with the luminescence. If we add more defects, we expect the luminescence to decrease proportionately. However, because the concentration of luminescent centers in the cerium-doped samples is less than the doping in the europium-doped samples, the probability of a new defect being close enough to the luminescent center to it is also smaller. Therefore, we expect a larger number of defects will be needed to quench the cerium doped samples. And in fact, the fluence, which we assume is proportional to the number of defects, required to quench the cerium-doped samples is about 6 times that of the europium-doped samples. The concentration of europium is also 6 times that of the cerium. Although the remarkable comparison of the difference in half-brightness dose to the difference in doping concentration is probably fortuitous, the foregoing analysis, nevertheless, suggests that the sensitivity of phosphors to radiation damage can be improved with doping as long as the doping concentration stays in the linear region.

The asymmetry ratio, R/O, does not show a trend as indicated in Figure 4.9 and Table 4.2. This result suggests that the red and orange emission peaks are affected without discrimination under proton irradiation. Furthermore, symmetry of the Eu^{3+}site does not

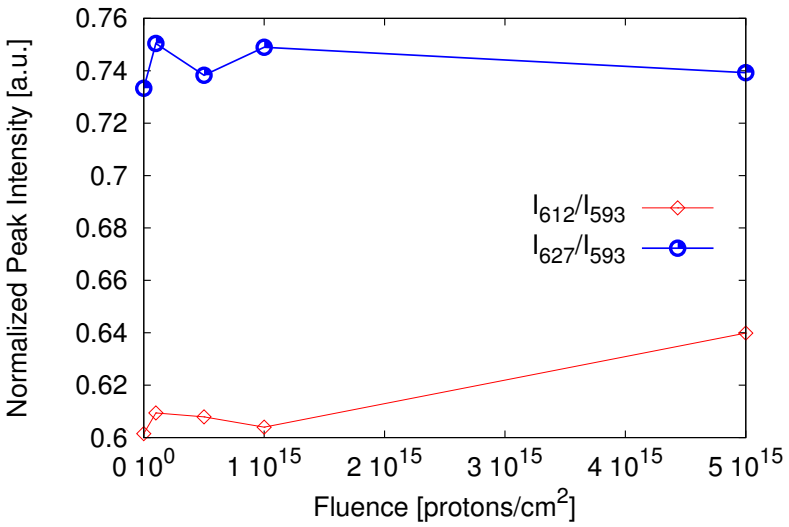

Figure 4.9 Ratio values of the red emission peaks at 612 nm and 627 nm ($^5D_0 \longrightarrow {}^7F_2$) over the orange emission peak at 593 nm($^5D_0 \longrightarrow {}^7F_1$) in YBO_3:Eu^{3+} as a function of proton fluence.

Table 4.2 R/O ratios from YBO_3:Eu^{3+}.

Fluence [protons/cm^2]	$I_{612\,nm}/I_{593\,nm}$	$I_{627\,nm}/I_{593\,nm}$
0	0.602	0.733
1×10^{14}	0.609	0.750
5×10^{14}	0.608	0.738
1×10^{15}	0.604	0.749
5×10^{15}	0.640	0.739

change significantly.

Preliminary results (from October 2012) were intriguing. We observed the expected effect in the photoluminescence, but unexpected effects in the lifetime measurements. We hypothesized that the photoluminescence and the lifetime would both decrease monotonically. Instead, the lifetime increased after the first proton irradiation step ($10^{14}\,H^+/cm^2$) and then decreased after each subsequent irradiation step. To determine whether this result was an error, we repeated the experiment (in February 2013), this time with the ideal

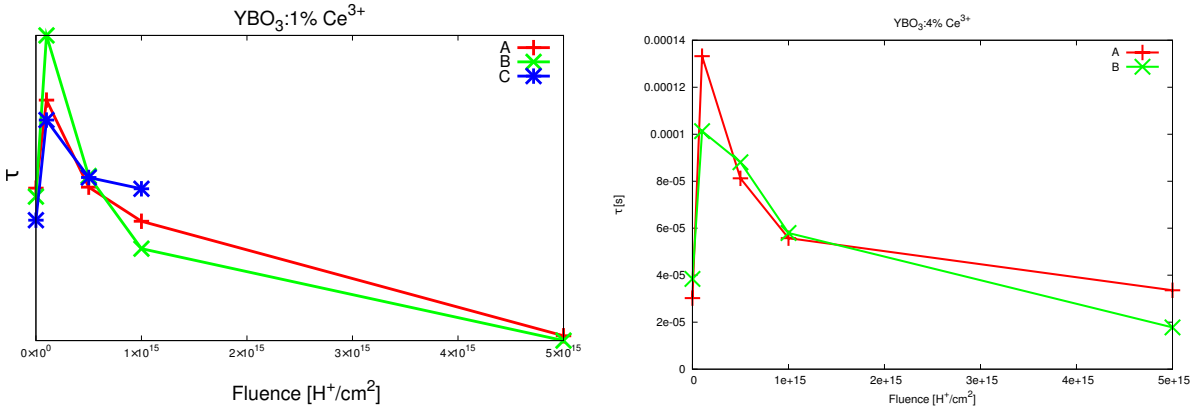

Figure 4.10 Preliminary decay results from (a) October 2012 on YBO_3:1%Ce^{3+} and (b) February 2013 of YBO_3:4%Ce^{3+} after 1 MeV proton irradiation.

dopant concentrations. The trends are the same in each set of tests.

We tested the same material at lower fluences to find the approximate threshold at which the photoluminescence intensity changed most significantly. The fluences tested were 10^{12}, 10^{13}, and $10^{14}\,H^+/cm^2$. The results were inconclusive because the photoluminescence emission intensities varied within the range of error. This test should be repeated with more careful experimental procedures.

In April 2013, we used 2 MeV protons instead of 1 MeV protons at fluences from 10^{14} to $3\times10^{15}\,H^+/cm^2$. Changing the proton energy could have an effect on the sensitivity of the material to irradiation. We expect higher energy protons to penetrate deeper into the material and cause more damage. The photoluminescence and decay measurements do not reflect the same trends as previous tests and the changes in emission intensities are within the noise. At this point we are at a loss to explain this result. During these experiments, the pelletron was unstable and provided an inconsistent beam current.

In the YBO_3:1%Ce^{3+} photoluminescence emission results shown in Figure 4.7 (a), we see the characteristic two-peak curve between 380 nm and 440 nm. The shape of the emission is the same for both pre- and post-irradiation spectra, meaning that if damage

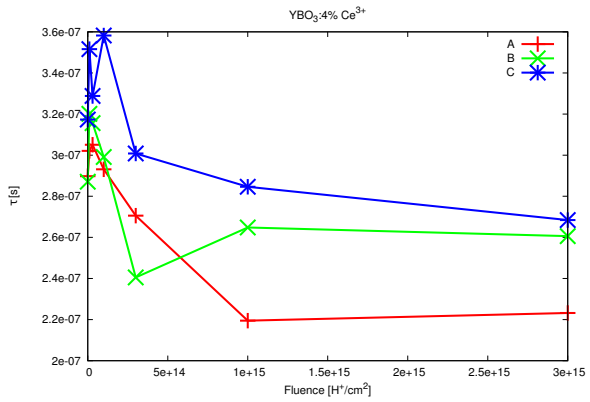

Figure 4.11 Decay results from April 2013 2 MeV proton irradiation on YBO_3:4%Ce^{3+}.

occurs, it does not affect one transition over another. The intensity of the post-irradiation spectra is significantly lower than the pre-radiation spectra by about 40%, suggesting that the radiation indeed produced damage that is evident in the photoluminescence.

The degradation of the photoluminescence emission could certainly be a result of radiation damage. Non-ionizing radiation damage mechanisms are conceptualized as billiard-ball interactions. A proton, which behaves like a high-energy particle, travels into the phosphor material and knocks another ion out of its lattice site. The loss of an ion or multiple ions changes the local environment of the luminescent center. In the cerium-doped YBO_3, we hypothesized that displacement would quench a number of luminescent centers making the normalized emission intensity degrade. On the other hand, we can not distinguish between a change in the absorptivity at the excitation wavelength and a change in the emission of the material. Nevertheless, a change in the spectrum due to radiation is clearly observed.

However, a change in the photoluminescence does not prove that the degradation is a direct result of radiation. Perhaps some the degradation is a result of hydrocarbon buildup from trace molecules in the vacuum chamber, or a surface contaminant that originates from the phosphor and blocks the interaction of photons with the phosphor. Although the results

are compelling, we are not prepared to claim with certainty that the degradation in the observed photoluminescence spectra is due to radiation-induced displacement damage.

The europium-doped phosphors are potentially more interesting because they emit line spectra rather than broad emissions. Line spectra have multiple narrow peaks representing various dipole transitions available in the structure. Since the peaks are narrower and more dependent on the crystal field, there are more opportunities to damage the material and the damage could be easier to detect. Upon investigation of the europium-doped YBO_3 spectra shown in Figure 4.7 (b), we see a similar degradation in the overall emission. We had hypothesized that changes in the spectra such as peak red- or blue-shifting, relative peak intensities changes, or emission shape changing (peaks appearing or disappearing completely) might be evident. This type of result might provide more information about the mechanisms of damage. For example, if the 611 nm peak degraded significantly, but the 627 nm and 593 nm peaks did not, we could postulate that the magnetic dipole transition is more susceptible to radiation damage than the electronic dipole transition. Even though these features are not observed, a degradation in the overall normalized intensity is still a compelling indication of radiation damage.

Change in Photoluminescence Spectra of YBO_3			
Ce emission λ	degradation	Eu emission λ	degradation
388 nm	39.1%	593 nm	49.6%
412 nm	40.8%	611 nm	57%
–	–	627 nm	47.7%

To understand the radiation effects and to develop a model for the observed changes, the first concept to consider is why the photoluminescence changes as a function of the activator concentration. In general, photoluminescence intensity increases linearly with activator concentration for dilute solutions. At low activator concentrations, luminescent

centers are too far apart to transfer their excitation energy to another activator or quenching center. Therefore, an excited center will remain excited until it emits a photon, and more excited activators results in more emission. In the dilute regime, the lifetime is unchanged with concentration. Because there is no energy transfer, each excited center emits independently, and the lifetime of the entire structure is uninfluenced by the number of emitters.

As the concentration of activators increases, the average distance between them decreases and can be approximated as twice the Wigner-Seitz radius

$$d = 2\left(\frac{3}{4\pi x_a}\right)^{1/3} \tag{4.2}$$

where x_a is the concentration of 3+ sites being occupied by an activator, that is $x_a = \text{mol}\%(12 \text{ atoms per unit cell})/(V_{UC})$. When d approaches a transfer distance, which depends on the material and transfer mechanism, the luminescence efficiency and lifetime can become dominated by quenching processes [70], and both decrease.

The luminescence emission rate is a function of radiative and non-radiative transition rates. Radiative transitions occur as emission of photons while non-radiative transitions occur through one or more of a combination of mechanisms: thermal relaxation, concentration quenching, or defect quenching. Mathematically, we can separate these transition rates into the sum of each mechanism using Matthiesen's rule.

$$\frac{1}{\tau} = \frac{1}{\tau_r} + \frac{1}{\tau_a} + \frac{1}{\tau_d} + \frac{1}{\tau_{th}}, \tag{4.3}$$

where radiative emission is designated by subscript r, quenching by defects as d, quenching by activator pairs as a, and thermal quenching as th. Thermal quenching occurs due to changes in the temperature and depends on the material. In our study, the tests were performed well below the temperature at which thermal de-excitation becomes significant, so the thermal quenching rate is neglected from here on. The overall lifetime, which can be measured directly, is given as [71]

$$\tau = \frac{\tau_r}{1 + \tau_r/\tau_a + \tau_r/\tau_d}. \tag{4.4}$$

The activator quenching rate is proportional to the activator concentration x_a. However, the relationship of the concentration to the quenching rate depends strongly on energy transfer between activators. For simple pair quenching, rates can be linearly dependent on concentration, but resonant transfer mechanisms can augment quenching so that the quenching rate depends on higher powers of the activator concentration. Although the power law for various transfer mechanisms (dipole-dipole, FRET, charge hopping, etc.) has been described [72], we can not distinguish between these mechanisms in our data; therefore, we will treat the power as an unknown fitting parameter such that $1/\tau_a \sim x_a^n$.

As defects are added, the probability that a new defect will be placed within a certain distance from an excited activator—the quenching distance r_q—is proportional to the volume occupied by all the activators divided by the total volume of the system. The volume occupied by activators is estimated as the concentration of activators multiplied by the volume of influence of a single activator.

$$P(\text{interaction}) = \frac{N\frac{4}{3}\pi r_q^3}{V} = x_a \frac{4}{3}\pi r_q^3 \tag{4.5}$$

The probability that a new activator interacts with a defect carries the same probability except that the number of defects is counted. Therefore, the defect quenching rate is $1/\tau_d \sim x_a x_d$. This model for concentration and defect quenching can be written as

$$\tau = \frac{\tau_r}{1 + C_1 x_a^n + C_2 x_a x_d} + \tau_{\text{off}}, \tag{4.6}$$

where C_1 and C_2 are fitting prefactors, and τ_{off} is a nominal decay time for large concentrations. This parameter is needed (we believe) to accommodate a varying Ce^{3+}/Ce^{4+} ratio [73].

Figure 4.12 shows the measured lifetimes of samples of YBO_3:Ce^{3+} with different

Table 4.3 Estimated parameters from Equation 4.3 for the fits shown in Figure 4.12.

	Proton Experiment	Concentration Quenching Experiment
parameter		
τ_r	41.2 ns	20.3 ns
C_1	1.64×10^4	7.7×10^7
n	3.42	5.80
τ_{off}	16.8 ns	0 ns

activator concentrations. One set of data show results (blue) from the same samples used in the radiation experiment where the measurements were taken prior to exposure to protons. Another set shows results (red) from a concentration quenching experiment performed separately. The samples were fabricated using the same recipe and synthesis method, but by different people. Differences can be explained by small variations during synthesis such as different muffle furnaces, contaminated or different sizes of crucibles, or a different purity or source of reactants [24, 74–76]. From the data, the fitting parameter C_1 can be estimated, but C_2 can not because there are no radiation-induced defects in this concentration quenching study. There are intrinsic defects like grain boundaries and impurities, which can form cationic quenching sites, but these are not included in the defect component of the quenching because natural defects are assumed to be constant throughout the experiment. Instead, the effects of these intrinsic quenching sites is included implicitly in the τ_r term.

Therefore the number of fitting parameters in Equation 4.3 is reduced to four: τ_r, C_1, n, and τ_{off}. The effects of these inherent defects are embedded in the τ_r parameter, which does not change with activator concentration. Table 4.3 provides the estimates of the fits that are shown in Figure 4.12. At 3 mol% doping ($Y_{0.97}Ce_{0.03}BO_3$), transfer mechanisms between luminescent centers begin to increase to the point where intrinsic defects are found more easily, so quenching is increased.

Doping concentration affects the overall emission intensity in addition to the decay time. For dilute systems, the emission intensity is proportional to the activator concen-

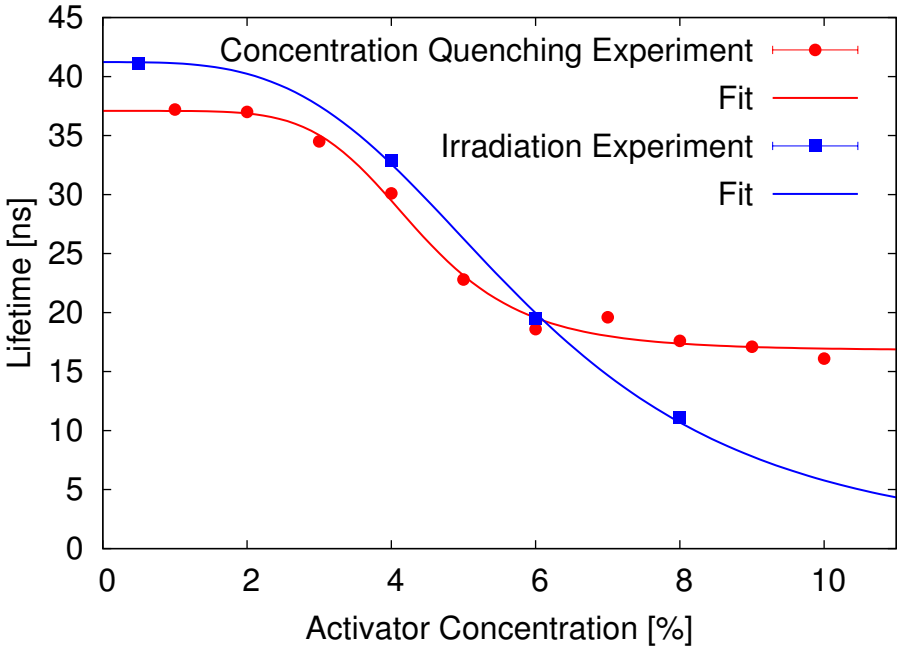

Figure 4.12 Lifetime as a function of activator concentration. Lines are from the fit of equation 4.3 without the defect term.

tration. As the concentration of activators increases to the point where energy transfer mechanism begin to dominate, the emission intensity decreases due to quenching much like the lifetime. A model for the normalized emission can be derived from Equation 4.3 by introducing the linear dependence of the emission on concentration.

$$\eta = \frac{\eta_0 x_a}{1 + C_1 x_a^n + C_2 x_a x_d}. \tag{4.7}$$

The magnitude of the intensity is obtained from spectral measurements of each sample. Figure 4.13 shows the emission spectrum and the fit of the measurement for the 1 mol% doping sample. The height (magnitude of the intensity), width, and location of the emission peaks are obtained by fitting Gaussians to the measurements. The peak at 365 nm is a reflection from the UV/VIS excitation. The emission intensity vs. concentration data

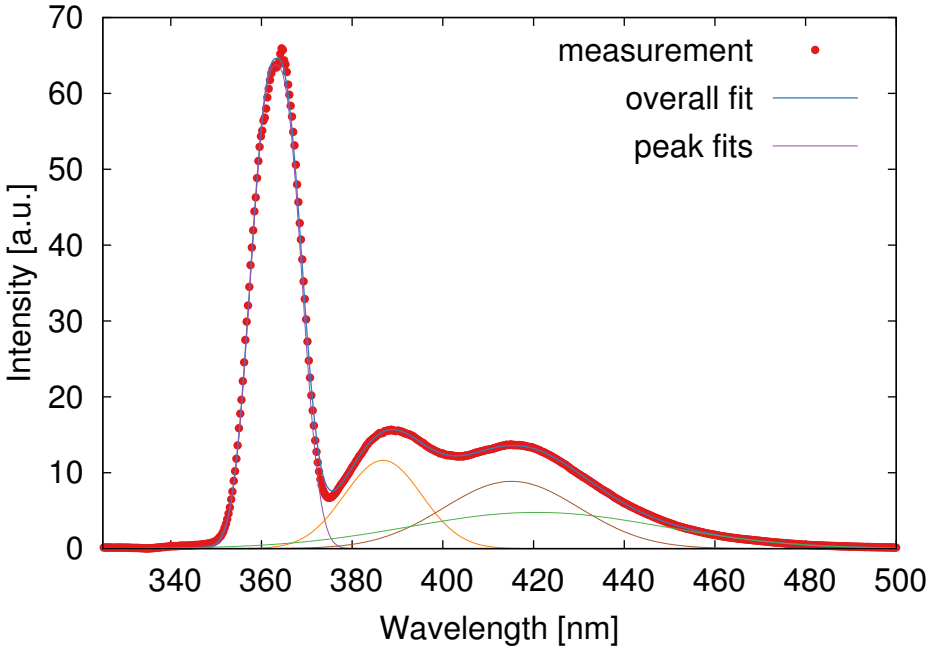

Figure 4.13 The parameters of the curves are obtained by fitting a Gaussian to each peak in the measurements. The data shown is from a 1 mol% doped sample.

in Figure 4.3 show that the 384 nm peak, which is the 5d-4f($^2F_{5/2}$) transition, reaches a maximum intensity at about 2 mol% cerium doping. The 414 nm peak, which is the 5d-4f($^2F_{7/2}$) transition, maximum is closer to 3 mol% cerium doping. The third peak is located at approximately 450 nm and is believed to be a result of Ce^{4+} in the material. Evidently, Ce^{4+} is a greater percent of the material in higher-doped samples [77–79].

The error bars in Figure 4.3 were obtained as the standard error of the peak intensity resulting from the fit. The magnitude of the bars gives an estimate of the random error in the spectral measurements. However, the variability in the data, in addition to the random noise in the spectral measurement, can be attributed to environmental differences arising from the fabrication, handling, and measurement of the various powder samples. For example, the combustion synthesis creates a powder whose grains may not contain the exact same doping level. We crush the powder into micron sized grains and mix the grains before mounting, so

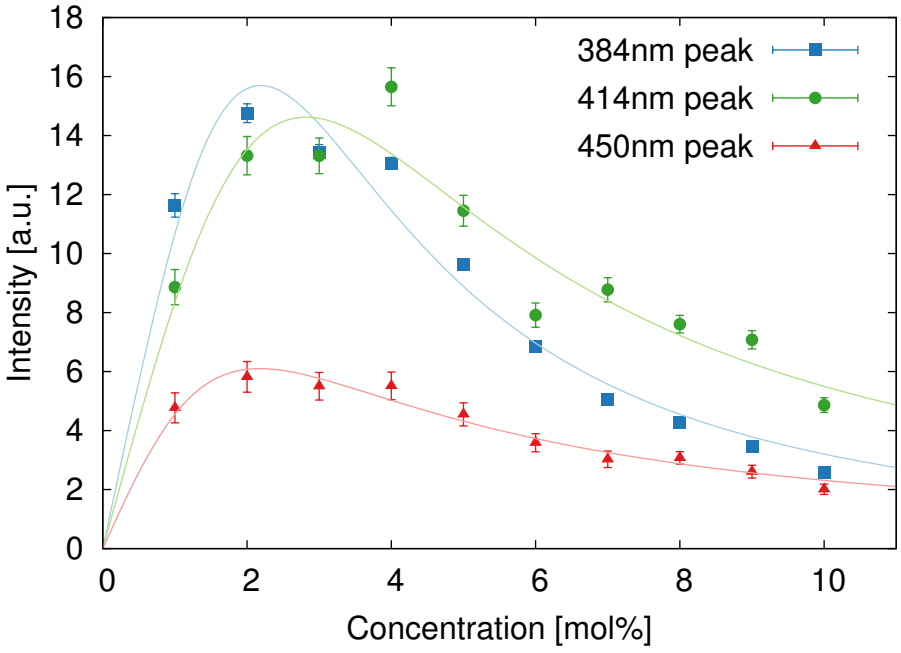

Figure 4.14 Photoluminescence emission concentration quenching curves of YBO_3:Ce^{3+} transitions 5d-4f($^2F_{5/2}$) (blue) and 5d-4f($^2F_{7/2}$) (green). The red peak is believed to be a Ce^{4+}. The fits are of Equation 4.3.

parameter	384 nm	414 nm	450 nm
η_o	11.5	8.84	5.39
C_1	7.37×10^{-2}	5.74×10^{-2}	18.1×10^{-2}
n	2.67	2.42	2.09

we expect the average doping to be at the stoichiometric doping level, but we can't control this variable better than a few percent [66].

The location of the maximum emission red-shifts slightly as the activator concentration increases as shown in Figure 4.15. This is due to crystal straining with an increase in substitution luminescent centers [28]. Furthermore, the ratio of the peaks (414 nm peak over 384 nm peak) increases with concentration. This suggests that the probability of the 5d-4f($^2F_{7/2}$) transition is higher than the 5d-4f($^2F_{5/2}$). The error bars associated with the

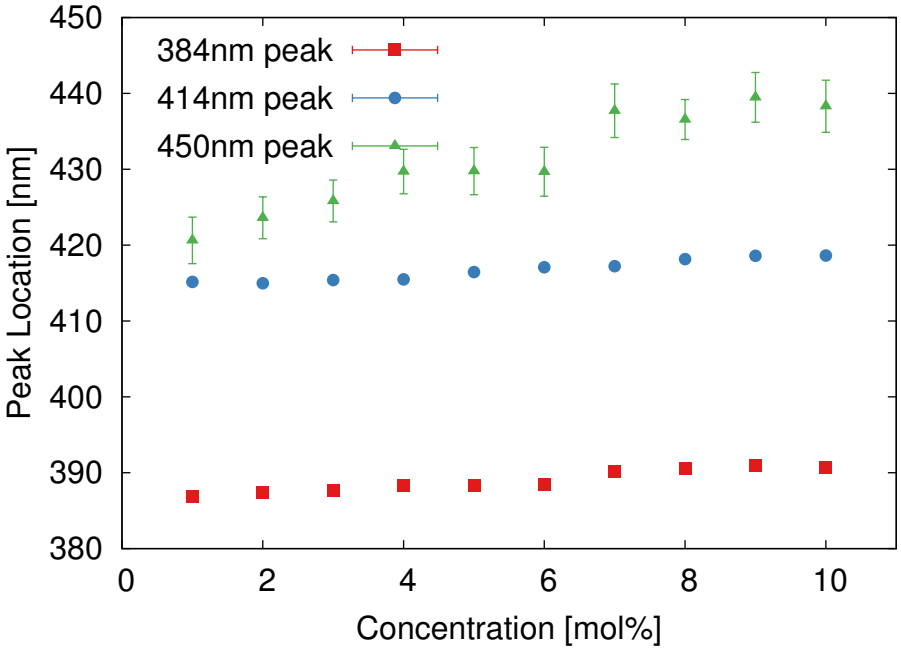

Figure 4.15 The maximum emission intensity at the 384 nm peak, 414 nm, and 450 nm peak in YBO_3:Ce^{3+} increases slightly with increasing Ce^{3+} concentrations.

location are obtained from the standard error of the fit as those in Figure 4.3. Because the peak shift is less sensitive to concentration, we don't see the systematic errors associated with intensity measurements.

There are two main reasons for the concentration quenching study. First, damage detection is easier with a stronger photoluminescence response than a weak response. Therefore, finding the optimal doping concentration allows changes to be detected in the measurements of both photoluminescence and decay easier. Second, these data can be used to get an estimate for τ_r and the pure concentration term prefactor C_1 and exponent n in equation 4.3 by fitting to the concentration quenching curve without the defect term.

The concentration quenching curve of YBO_3:Ce^{3+} in Figure 4.3 shows that photoluminescence intensity increases monotonically from a concentration of 0 mol% to about 3 mol%, where the emission is a maximum. Doping concentrations higher than 3% result in

more activator quenching and thus the emission intensity decreases. All three peaks shown in the figure of the cerium emission follow the same trend. However, the measurements and corresponding model are not detailed enough to isolate the effects of the different sites. The model does not distinguish whether the emission source is from a 5d-4f($^2F_{7/2}$) transition site or a 5d-4f($^2F_{5/2}$) transition site. Furthermore, the 5d-4f($^2F_{7/2}$) transition level could be excited but non-radiatively decay to the a 5d-4f($^2F_{5/2}$) transition level which could then emit or quench.

The results of the proton irradiation step-stress experiment are shown in Figure 4.16 and Figure 4.17. The maximum emission intensity of the 384 nm peak decreases as a function of fluence and follows the trend described by Birks and Black. The decay of YBO_3:Ce^{3+} doped at 0.5 mol%, 4 mol%, 6 mol%, and 8 mol% Ce^{3+} are plotted as a function of fluence in protons/cm^2. Each data point is the average of three samples, all of which were exposed to radiation and measured the same way.

The pre-radiation data in Figure 4.17 are fit with Equation 4.3 using C_1, n, and τ_r, where $C_2 = \tau_{\text{off}} = 0$. Each set of data, 0.5 mol%, 4 mol%, 6 mol%, and 8 mol%, has a different pre-irradiation decay time determined by the concentration. As the concentration of activators increases, the decay time decreases—more activators leads to faster decay due to pair-quenching. This effect is demonstrated in the lifetime concentration quenching curve (see Figure 4.12). We assume that there are no differences in the number of defects (intrinsic or radiation-induced) at a fluence of 0 protons/cm^2 for each concentration; therefore, the fit parameters are constant from the pre-radiation data. In our experiment, we systematically introduced defects with particle radiation. What we can't do is map the number of defects to the fluence. All our radiation effects are, therefore, plotted as a function of fluence (not defect concentration). In the model, we assume that the un-irradiated sample is defect free. Of course, this is not realistic, but the effects of the intrinsic defects can be captured in the τ_r term (as stated previously), which is estimated at $x_d = 0$. Consequently, when we refer to defects being introduced, we are referring to the defects introduced over

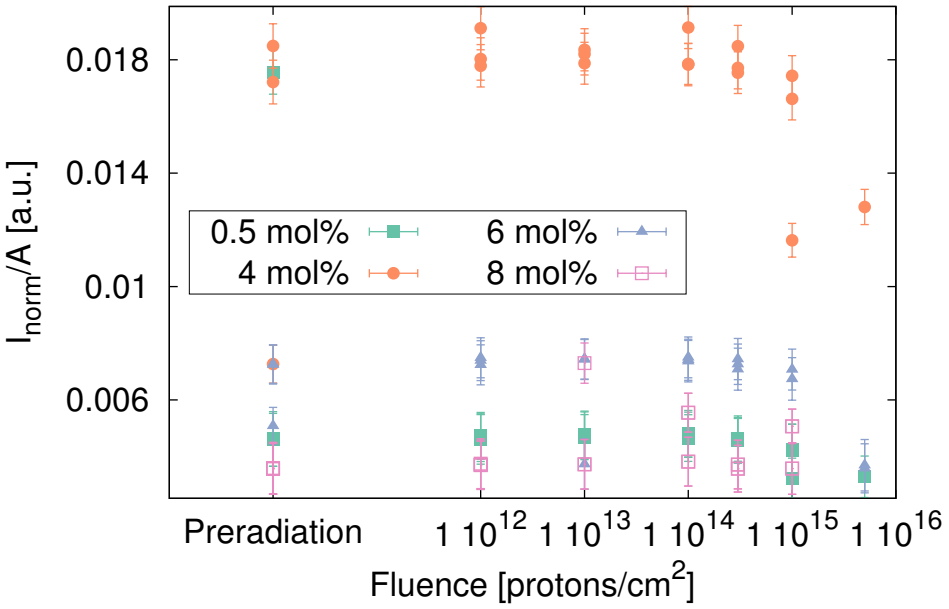

Figure 4.16 The maximum normalized emission intensity of the 384 nm peak divided by the area of the reflection of the excitation as a function of fluence at 0.5 mol%, 4 mol%, 6 mol%, and 8 mol% activator concentration.

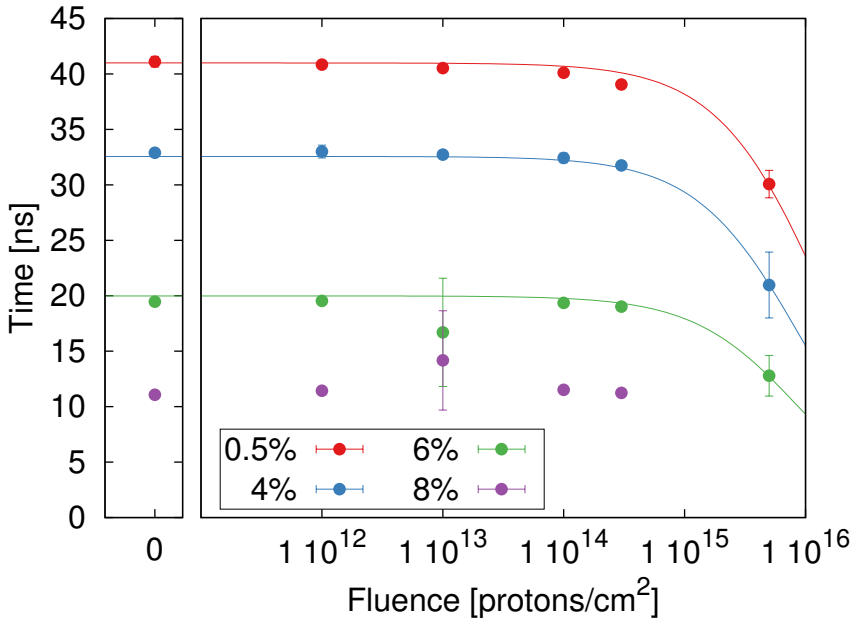

Figure 4.17 Decay time of YBO_3:Ce^{3+} as a function of fluence at 0.5 mol%, 4 mol%, 6 mol%, and 8 mol% activator concentration.

Table 4.4 Estimates of the prefactor for the influence of radiation-induced displacement damage from the fits in Figure 4.17.

mol%	C_2 (cm^2)	std. err. (cm^2)
0.5	1.48×10^{-14}	1.06×10^{-15}
4	3.46×10^{-15}	1.38×10^{-16}
6	3.92×10^{-15}	1.26×10^{-15}

and above the intrinsic defect level.

The results of the fit are given in Table 4.3 for the proton experiment. Consequently, the lifetime for un-irradiated samples ($x_d = 0$) were $\tau(x_a = 0.5) = 41.0\,\text{ns}$, $\tau(x_a = 4\%) = 32.6\,\text{ns}$, $\tau(x_a = 6\%) = 20.0\,\text{ns}$, and $\tau(x_a = 8\%) = 10.7\,\text{ns}$. We then fix the values of C_1, n, and τ_r for the subsequent fit of C_2 using the measurements from the irradiated samples. All samples have an approximately constant lifetime until around the third irradiation ($\sim 1 \times 10^{14}\,\text{protons/cm}^2$). The 8 mol% sample was inadvertently damaged before testing at the largest fluence where the radiation-induced displacement damage becomes significant. Therefore, a fit of this sample is not meaningful.

The decrease in lifetime at higher fluences can be attributed to quenching that results from radiation-induced defects. We can see a dramatic decrease in lifetime between the $x_d = 3 \times 10^{14}\,\text{cm}^{-2}$ and $x_d = 5 \times 10^{15}\,\text{cm}^{-2}$ at all concentrations. The lifetime of the 0.5 mol% sample dropped 8.9 ns (23%), that of the 4 mol% dropped 10.8 ns (34%), and that of the 6 mol% sample dropped 6.2 ns (33%). Clearly, the higher concentrations (above the optimal concentration of 3 mol%) are more sensitive to small changes in fluence. However, Table 4.4 shows the C_2 value from the fit. The lower concentration ($x_a = 0.5\,\text{mol\%}$) is affected by the radiation at a lower fluence ($1/C_2 = 6.8 \times 10^{13}\,\text{cm}^{-2}$) than the $x_a = 4\,\text{mol\%}$ and $x_a = 6\,\text{mol\%}$, which are affected at $2.9 \times 10^{14}\,\text{cm}^{-2}$ and $2.6 \times 10^{14}\,\text{cm}^{-2}$ respectively.

4.4 Neutrons, Tetrakis, and Future Work

The neutron experiment took place at OSU, so without the spectroscopy equipment from Vanderbilt we could not take measurements between irradiations. Instead, we irradiated samples for different durations. We had two sets of samples: one set had the powder mounted in the aluminum squares like the other experiments, and the other set had unmounted powder in 0.3 mL polyethylene vials. Three mounted samples were irradiated at each of four fluences—10^{12}, 10^{13}, 10^{14}, and 10^{15}, plus three controls (unirradiated). There were two vials of loose powder for each fluence. All of them samples were packed into a polyethylene bottle and padded with cotton. The cotton was supposed to help prevent the powder from coming out of the mounted samples when the bottle was thrust into and out of the rabbit facility. Unfortunately, not many of the mounted samples survived. No decay measurements were taken for this set of experiments.

The photoluminescence emission was measured by creating a 3-D-printed piece which has a well in it which fits the vials. The rest of the setup remained the same. The distance from the fiber to the sample powder in the vial was enough to ensure that only the powder was hit by the beam. However, since the vial reflected the excitation/emission, a background of an empty vial was subtracted from the results. The photoluminescence measurements from the vial samples do not seem to show a trend.

From the surviving mounted samples, we could create a compelling set of results, but these should not be seen as conclusive.

Because the europium tetrakis (EuD_4TEA) has such high light yield and seems to emit under weak effort (just tapping the powder with a spatula), we thought it might be sensitive to even low-fluence radiation like alpha particles. We tested the tetrakis under ^{241}Am and then also ^{210}Po over a period of several days. The ^{210}Po source has an activity of 500 μCi, which is much larger than the ^{241}Am sources (one has 0.1 μCi and the other has 10 μCi. The fluence from ^{210}Po corresponds to 1.11×10^{16} per day. These results are inconclusive and the experiment should be repeated.

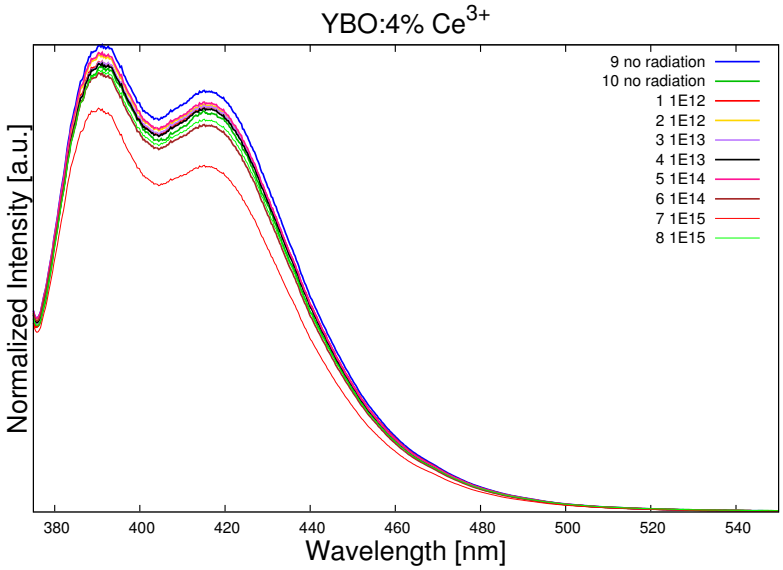

Figure 4.18 Photoluminescence emission from vial samples of YBO_3:4%Ce^{3+} after neutron irradiation.

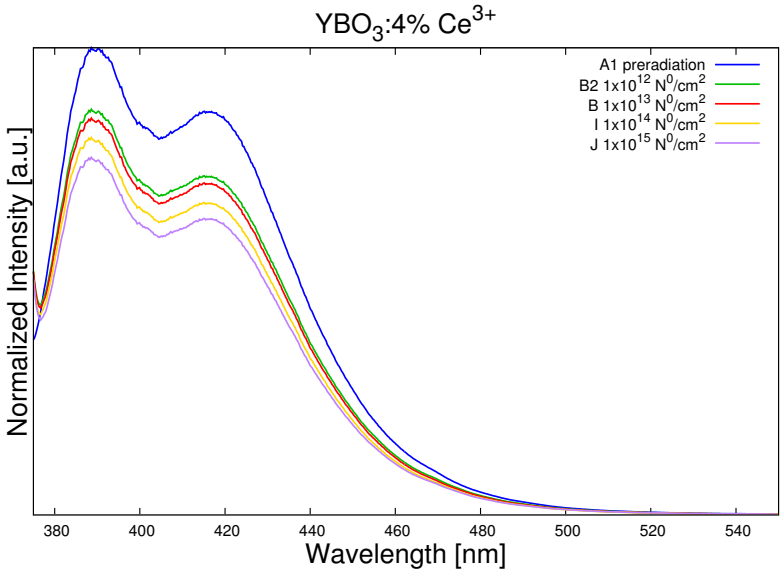

Figure 4.19 Selection of results from OSU neutron experiments–mounted samples of YBO_3:4%Ce^{3+}.

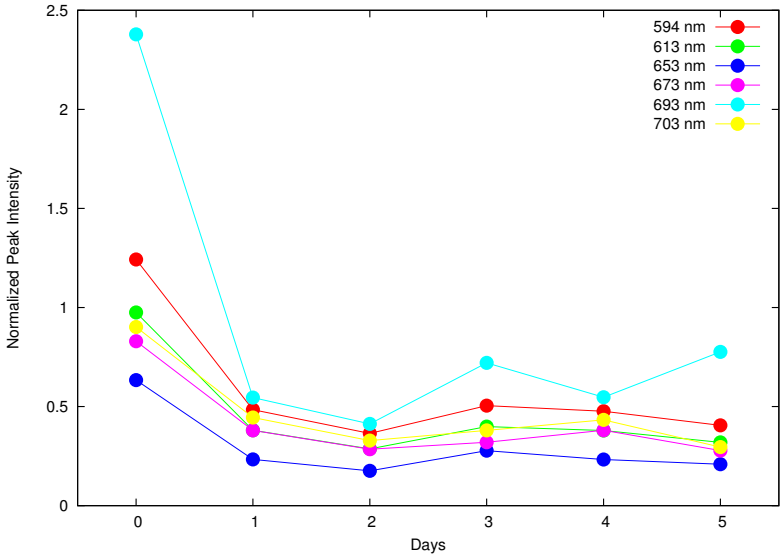

Figure 4.20 ^{210}Po irradiation of EuD_4TEA.

CHAPTER V

CONCLUSIONS

This research provides a method to study radiation-induced displacement damage in materials through photoluminescence. This is a unique approach because most studies using phosphors focus on their scintillation. More importantly, in addition to using the emission spectrum as a means of detecting displacement damage, we look at the lifetime, which has not been done in YBO_3 before. In fact, we only came across one other publication that considered lifetime as a means of detection for displacement damage–"In situ variations of carrier decay and proton induced luminescence characteristics in polycrystalline CdS" by Gaubas et al. [40].

Radiation that is primarily ionizing, such as x-rays, does not cause permanent displacement damage, at least not at low intensities. And alpha radiation did not damage our phosphors, at least not enough to be detected by photoluminescence. However, higher fluences should be tested to determine what level of radiation affects the photoluminescence. While high-fluence ionizing radiation may change the optical properties of phosphors, it does not cause permanent displacement damage than can be used as a record after a long time. Non-ionizing energy loss (NIEL) is more likely to cause permanent damage to the phosphor that can be detected long after the creation of the damage.

Our original hypothesis was based on the dependence of the luminescence on the local crystal environment. In particular, we expected Ce^{3+} to respond to defects more dramatically because luminescence from Eu^{3+} is essentially independent of the lattice. Ce^{3+} emission, on the other hand, arises due to the lattice structure. Therefore, if we damage the lattice, we expect something about the spectrum of YBO_3:Ce^{3+} to change differently compared to the spectrum of YBO_3:Eu^{3+}. However, our observations did not support this

hypothesis. We indeed measured a degradation in the intensity and lifetime, but we did not observe any significant shifts in either spectrum. Instead, our data indicate an overall degradation of the emission intensity regardless of the local crystal environment. This suggests that defects act primarily as quenching sites and do not strain the crystal such that the photoluminescence emission changes.

The most recent work on proton-irradiated YBO_3:Ce^{3+} demonstrates a strong relationship between radiation-induced displacement damage and photoluminescence lifetime. We assumed that fluence is linearly proportional to the number of defects in the material. After a critical fluence the lifetime decreases. This feature can also be seen in scintillating systems where the intensity is measured as a function of radiation dose. However, we also discovered that the initial activator doping alters the critical fluence such that lower doping levels are more sensitive to the fluence or corresponding number of defects. Furthermore, we were able to use Dexter's lifetime model on our data to differentiate between quenching mechanisms innate to the material and quenching mechanisms that were created by proton-induced defects. In summary, we have demonstrated that the lifetime of YBO_3:Ce^{3+} is a more robust measure of irradiation-induced damage than normalized emission spectra. YBO_3:Ce^{3+} is one of numerous phosphors and there is potential for developing a material that is more sensitive, perhaps by incorporating a sensitizer or using a single-crystal rather than a powder. The fluence required to create detectable displacement damage in YBO_3:Ce^{3+} is relatively high, but it could be possible to find a phosphor or combination of phosphors which have a much lower, more applicable, threshold for damage.

APPENDIX

5.1 Thermographic Phosphor Calibration

5.1.1 Methods

Temperature dependence of YAG:Dy and YAG:Tm were studied in collaboration with J. Eldridge, T. Jenkins, and S. Allison. Our contribution focused on developing a calibration curve for the materials to compare with results from other high-temperature experiments. The powder sample was placed in a small round-bottom ceramic crucible. The crucible was placed on top of a taller cylindrical crucible so that the sample was close to the opening at the top of the oven to maximize the solid angle between the emitting powder and the collection optics.

Two different phosphor samples were tested in this effort. The sample tested for the high temperature calibration was YAG:1%Tm from Phosphor Technology QMK69/N-X Lot 20236. The powder sample was 0.249 g placed in a small round-bottom ceramic crucible. The crucible was placed on top of a taller cylindrical crucible so that the sample was close to the opening at the top of the oven to maximize the solid angle between the emitting powder and the collection optics.

The excitation laser is a Continuum Surelite III, flashlamp pumped Nd:YAG with a pulse-rate of 10 Hz. The third harmonic at 355 nm, with a pulse duration of 8 ns was used for excitation. The beam is steered to the oven through three uncoated prisms, and the combined efficiency of getting the light into the oven is 5% providing 150 μJ at the oven, which is sufficient for excitation.

To direct the excitation beam to the sample and to collect fluorescence from the same access port, we used an uncoated plane window (flat piece of BK7 glass) at 45° to permit broadband transmission ($> 90\%$) as well as significant reflection (9%) of the excitation beam. An aperture is placed between the collection optics (600 μm fiber) and the plane window to limit ambient PMT illumination. Notch filters were placed ahead of the collimation optic, which were used to focus the emission onto the fiber.

The emission was collected with a 5 V Hamamatsu model H10721-20 PMT with 50 Ω terminator and interpreted by a LeCroy WaveSurfer 44MX-s-B oscilloscope. Averaging was done by triggering the scope on each laser shot using the Q-switch trigger. See Figure 5.1 for the laser and oven setup.

At each temperature the decay was measured with a 458 nm notch filter and a 365 nm notch filter. The gain was set to 600 mV for most samples measured with the 458 nm filter and 700 mV for most of the samples measured with the 365 nm filter. There is also an iris in the tube with the filters and the fiber coupler that was closed slightly for saturated signals (usually with the 458 nm filter). Each decay is the average of 100 pulses.

5.1.2 Results

Figure 5.2 shows the result for the instance of a long gate scanned out for almost 2.5 ms. There is clearly a short component and a long component to the decay of the emission. A narrower gate is necessary to better depict the shorter component. For this

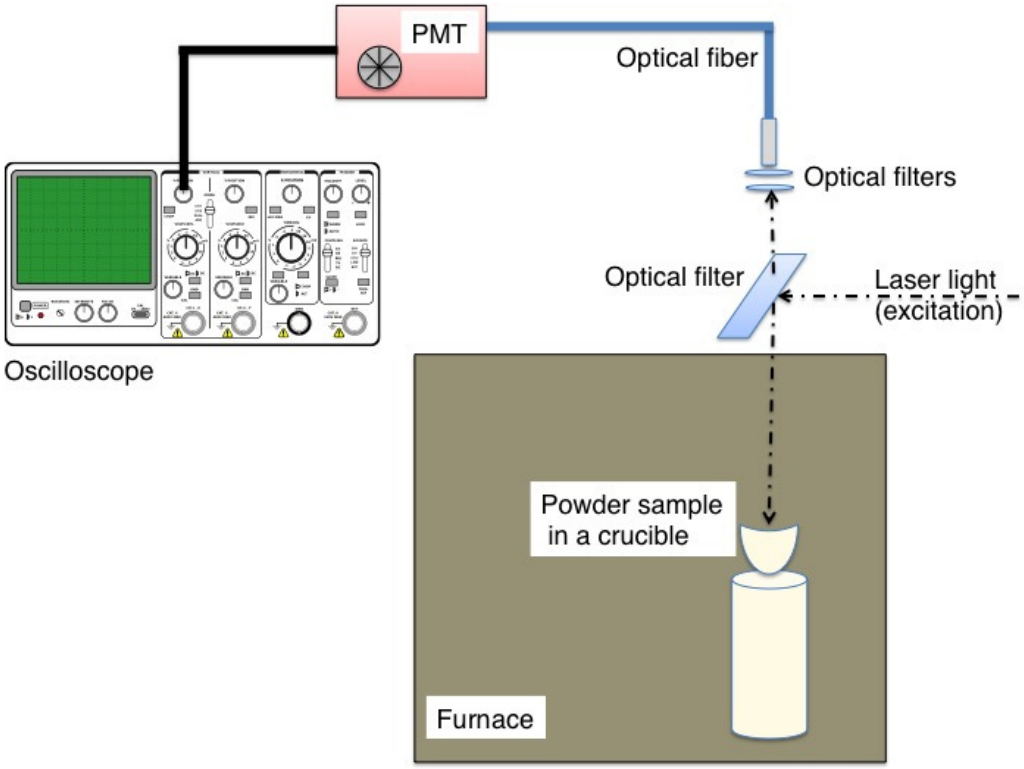

Figure 5.1 Oven showing the PMT orientation and laser input along with a depiction of the support on the interior of the oven.

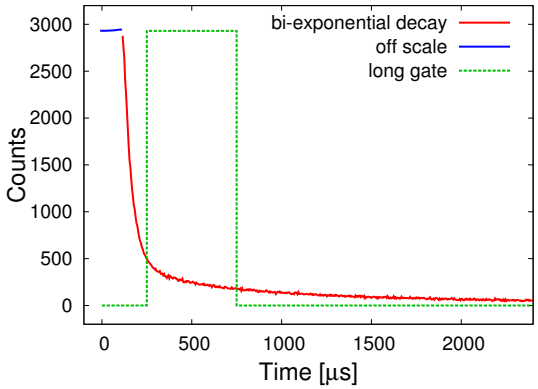

Figure 5.2 Example of YAG:0.8%Tm time dependence at 458 nm. Data provided by Steve Allison.

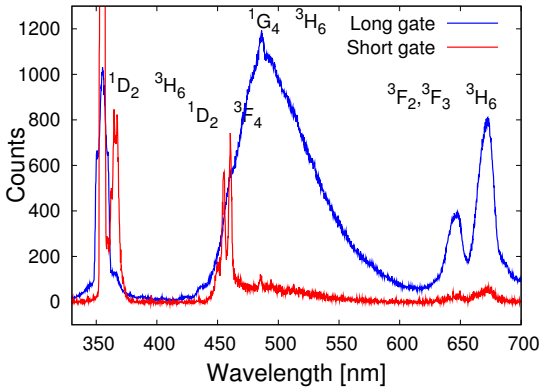

Figure 5.3 Example of YAG:0.8%Tm spectra for short and long gates. Data provided by Steve Allison.

run, the early part of the short component is off-scale; but, this setting was necessary to better show the longer component.

To obtain spectra, a gate width and its delay with respect to the excitation pulse were defined and the signal measured as the wavelength was scanned. Figure 5.3 shows the strikingly different results that were obtained for two different gate widths. Both were set to a delay of 40 μs to make sure the flash-lamp excitation had completely terminated. For short gate width, 150 μs, the spectral emission, indicated by the red trace, comes mainly from the $^1D_2 - ^3H_6$ and $^1D_2 - ^3F_4$ transitions. At least two Stark components are resolved at each position. Guy [56] lists five Stark components and greater spectrometer resolution might reveal these. The band at 365 nm is very close to the excitation at 355 nm and scattering in the spectrometer may obscure part of this band. For the long gate width, 1000 μs, the emission is predominantly from the $^1G_4$ with a peak at 486 nm and with significant emission within the 458 nm band. The spectral bandwidth was 1.5 nm.

Decay time, τ, was estimated from the time-resolved intensity after testing several fitting approaches. To begin, it was assumed the decay was characterized by a single exponential equation of the form $Aexp(-t/\tau)$ where A is signal amplitude and t is time. Next, a double exponential fit, the sum of two such equations, was executed. Similarly, a triple exponential fitting was performed. The decay traces of two longer wavelength emissions (458 nm and 486 nm) show strong multi-exponential behavior. Figure 5.4 (a) shows the luminescence signal at 300°C for the 365 nm peak. Figure 5.4 (b) shows the luminescence signal at 300°C for the 458 nm peak. The double fit was able to isolate fast transients (of the order of tens of nanoseconds) apparent in the data. Therefore, the characteristic thulium decay is slightly longer for the double fit. In general, the standard error of the double fit is smaller than the error for the single fit. Also, depicted are triple exponential fits, which turned out to be very similar to that of the double fit. This suggests that only two exponentials are required to faithfully capture the decay signal.

The multi-exponential character indicates that cascading may be involved with the

458 nm band. The replenishment ratio, which is defined as the rate at which the level is refilled from a higher level to the rate at which the level emits [80], is estimated from the bi-exponential fit parameters to 0.45. This refilling is presumably from the short-lived $^1D_2$. This indicates that the emission at 458 nm replenishes one of every two decays initially, which confounds the analysis of the decay of the 458 nm band. Consequently, the 365 nm peak may be a better wavelength for temperature measurements because it is less likely to contain multi-exponential behavior.

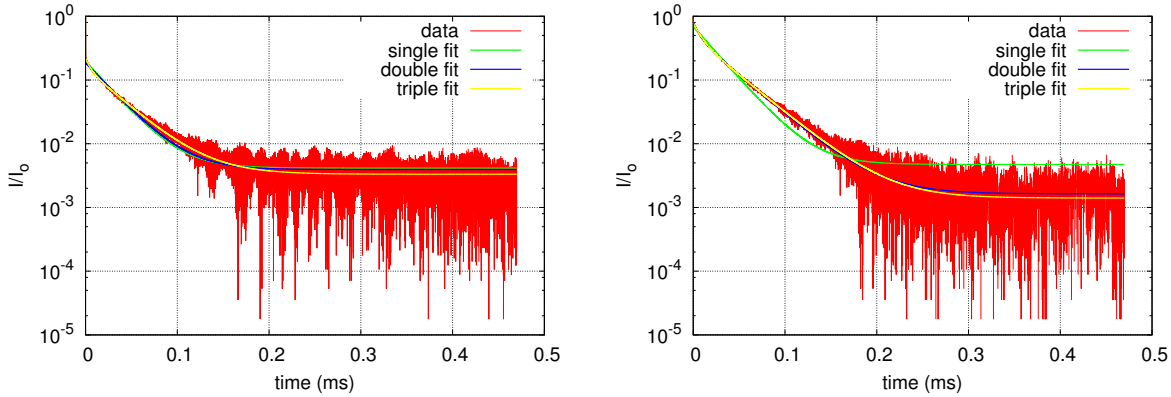

Figure 5.4 Semi-log plot of intensity vs time for (a) 365 nm and (b) 458 nm bands at 300°C with various fits as noted.

In order to obtain a calibration, decay times are determined over a range of temperatures. Exponential fits of the time-resolved emission show characteristic tens of microseconds decay times for both peaks and quenching temperatures were around 1000°C (see Figures 5.5 and 5.6). After the quenching temperature, the decay time decreases with increasing temperature to a decay time < 200 ns at temperatures greater than 1200°C giving a good sensitivity for temperature measurement. Near 1400°C, the decay curve reduces to a few nanoseconds, which is likely the decay of the laser and no additional information about the phosphor decay is apparent at these temperatures.

The decay time versus temperature calibration of the 365 nm band is very similar to 458 nm band. The decay time is essentially constant to about 1000°C at which point the temperature dependence is pronounced. With that established, there are at least two advantages to using the 365 nm band. One is that blackbody emission is less in the ultraviolet. As illustrated by the two spectra, the emission at 458 nm consists of emission from two states, $^1D_2$ and $^1G_4$, which adds complexity to analysis. Moreover, these states can be re-filled by higher energy states, further confounding measurements.

There are a number of additional features that should be explored in future work.

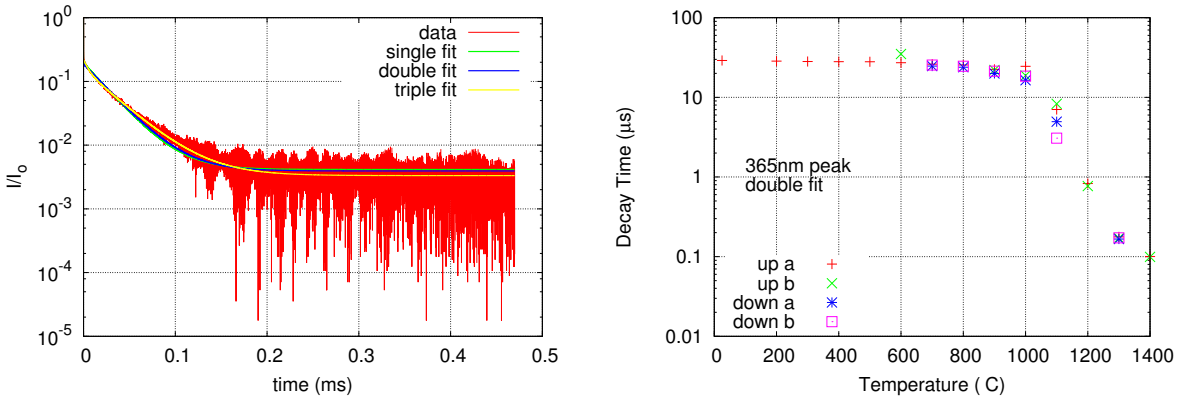

Figure 5.5 Calibration curves for 365 nm peak of YAG:Tm powder using (a) single exponential fit and a (b) double exponential fit.

It needs to be determined if the temperature dependence of the $^1G_4$ state is similar to the long-lived states characterized by Zhang [53,57] which show temperature dependence over a wide range. If so, then both long and short fluorescence emissions may be used in a complementary way for covering a wide range with lower sensitivity but high sensitivity at high temperatures.

The attention of this work focused on Tm in the YAG host. However, the results should be instructive for Tm in other hosts and serve at a starting point for exploring them. It is to be expected that in other hosts, the quenching temperature of the $^1D_2$ state will be different. Otherwise, decay times should be similar and have similar temperature dependence.

Another aspect that requires additional consideration is band intensity versus temperature and also versus excitation wavelength. Khalid and Kontis [81] explored this for several thermographic phosphors including YAG:Tm. They characterized the initial emission amplitude versus temperature and found that for the 458 nm band, the amplitude increased up to around 1000°Cand from there began to decrease when excited at 355 nm. When excited by 266 nm, the efficiency is less and the amplitude decreases with temperature. Will emission amplitude at 365 nm behave the same for these excitation wavelengths?

Lastly, there are higher lying states, $^1I_6$ and several ^{3}Ps, that may be accessed by excitation at 266 nm. Will the quenching temperature be precipitous like the $^1D_2$ or more gradual and cover a longer temperature range like the $^3H_4$ and $^3F_4$ states. Will it occur at a higher temperature? Even if there is no temperature dependence in certain ranges, the existence of so many states expands the possibility that temperature may be determined from the ratio of spectral emission amplitudes.

This work is an important step in advancing the utility of this material for high temperature measurements. The complexity of this phosphor shows that careful and extensive characterizations are necessary to fully exploit this material for phosphor thermometry.

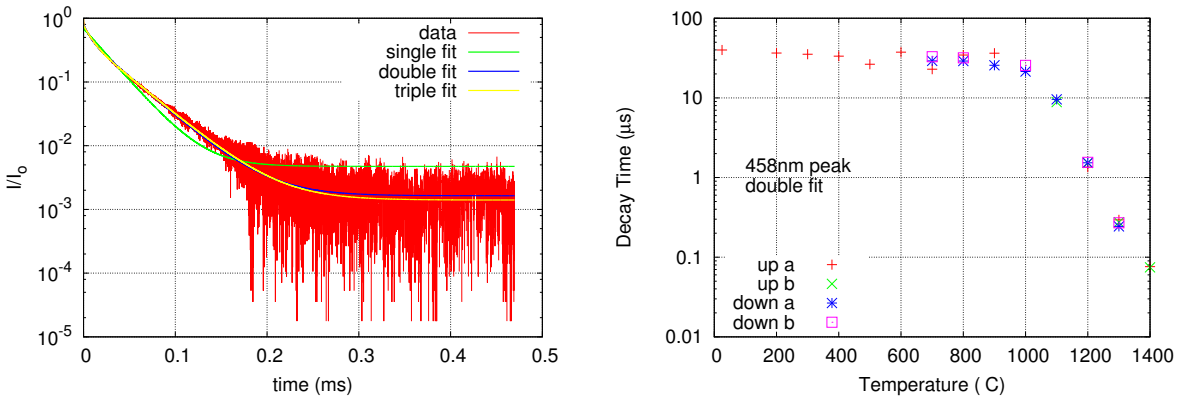

(a) (b)

Figure 5.6 Calibration curves for 458 nm peak of YAG:Tm powder using (a) single exponential fit and a (b) double exponential fit.

BIBLIOGRAPHY

[1] K Xia, R Reuter, R Stöhr, A Zappe, J Meijer, P R Hemmer, J Wrachtrup, and R Kolesov. Optical detection of a single rare-earth ion in a crystal. *Nature Communications*, 3:1029–7, August 2012.

[2] Masaaki Hirayama, Noriyuki Sonoyama, Atsuo Yamada, and Ryoji Kanno. Relationship between structural characteristics and photoluminescent properties of $(La_{1-x}Eu_x)_2M_2O_7$ (M=Zr, Hf, Sn) pyrochlores. *Journal of Luminescence*, 128(11):1819–1825, November 2008.

[3] Jianhua Lin, Denis Sheptyakov, Yingxia Wang, and Peter Allenspach. Structures and phase transition of vaterite-type rare earth orthoborates: A neutron diffraction study. *Chem. Mater.*, 16(12):2418–2424, June 2004.

[4] F P Mooring, J E Monahan, and C M Huddleston. Neutron cross sections of the boron isotopes for energies between 10 and 500 keV. *Nuclear Physics*, 82(1):16–32, 1966.

[5] D Boyer, G Bertrand, and R Mahiou. A spectroscopic study of the vaterite form YBO_3:Eu^{3+} processed by sol-gel technique. *Journal of Luminescence*, 104(4):229–237, August 2003.

[6] Thomas Jüstel, Jean-Claude Krupa, and Detlef U. Wiechert. VUV spectroscopy of luminescent materials for plasma display panels and Xe discharge lamps. *Journal of Luminescence*, 93(3):179–189, 2001.

[7] A. Mayolet, J.C. Krupa, I. Gerard, and P. Martin. Luminescence of Eu^{3+} doped materials excited by VUV synchrotron radiation. *Materials Chemistry and Physics*, 31(1–2):107–109, 1992.

[8] M. Ren, J. H. Lin, Y. Dong, L. Q. Yang, M. Z. Su, and L. P. You. Structure and phase transition of $GdBO_3$. *Chemistry of Materials*, 11(6):1576–1580, 1999.

[9] Mika Tukia, Jorma Hölsä, Mika Lastusaari, and Janne Niittykoski. Eu^{3+} doped rare earth orthoborates, RBO_3 (R=Y, La and Gd), obtained by combustion synthesis. *Optical Materials*, 27(9):1516–1522, July 2005.

[10] JinDeng Chen, Hai Guo, ZhengQuan Li, Hao Zhang, and YiXi Zhuang. Near-infrared quantum cutting in Ce^{3+}, Yb^{3+} co-doped YBO_3 phosphors by cooperative energy transfer. *Optical Materials*, 32(9):998–1001, 2010.

[11] L. Lou, D. Boyer, G. Bertrand-Chadeyron, E. Bernstein, R. Mahiou, and J. Mugnier. Sol-gel waveguide thin film of YBO_3: preparation and characterization. *Optical Materials*, 15(1):1–6, 2000.

[12] A. Majchrowski, J. Ebothé, I. Fuks-Janczarek, M. Makowska-Janusik, B. Sahraoui, and I.V. Kityk. Two-photon absorption in YAB:Cr^{3+} nanocrystallites. *Optical Materials*, 27(4):675–678, 2005.

[13] M J Knitel, P Dorenbos, CWE Van Eijk, B Plasteig, B Viana, A Kahn-Harari, and D Vivien. Photoluminescence, and scintillation/thermoluminescence yields of several Ce^{3+} and Eu^{2+} activated borates. *Nuclear Instruments and Methods in Physics Research Section A: Accelerators, Spectrometers, Detectors and Associated Equipment*, 443(2):364–374, 2000.

[14] C W E van Eijk. Inorganic-scintillator development. *Nuclear Instruments and Methods in Physics Research Section A: Accelerators, Spectrometers, Detectors and Associated Equipment*, 460(1):1–14, 2001.

[15] Jan Brübach, Christian Pflitsch, Andreas Dreizler, and Burak Atakan. On surface temperature measurements with thermographic phosphors: A review. *Progress in Energy and Combustion Science*, 39(1):37–60, February 2013.

[16] M D Chambers and D R Clarke. Doped oxides for high-temperature luminescence and lifetime thermometry. *Annu. Rev. Mater. Res.*, 39(1):325–359, August 2009.

[17] G Blasse and B C Grabmaier. *Luminescent materials*. Springer-Verlag, 1994.

[18] M R Cates, S W Allison, S L Jaiswal, and D L Beshears. YAG:Dy and YAG:Tm fluorescence above 1400°C.

[19] J L Wu, G Gundiah, and A K Cheetham. Structure-property correlations in Ce-doped garnet phsophors for use in solid-state lighting. *Chemical Physics Letters*, 441(4–6):250–254, 2007.

[20] Rachael A Hansel, S W Allison, and D G Walker. Temperature-dependent luminescence of Ce^{3+} in gallium-substituted garnets. *Appl. Phys. Lett.*, 95(11):114102, 2009.

[21] A. Tiwari, A.K. Mishra, H. Kobayashi, and A.P.F. Turner. *Intelligent Nanomaterials*. Wiley, 2012.

[22] J P Duignan, IDH Oswald, I C Sage, and L M Sweeting. Do triboluminescence spectra really show a spectral shift relative to photoluminescence spectra? *Journal of Luminescence*, 97(2):115–126, 2002.

[23] Dalai Jin, Xiaojing Yu, Xiaoqin Xu, Lina Wang, Longcheng Wang, and Naiyan Wang. Hydrothermal synthesis of amorphous spherical-shaped YBO_3:Eu^{3+} and its photoluminescence property. *J Mater Sci*, 44(22):6144–6148, September 2009.

[24] Xianwen Zhang, Archis Marathe, Sandeep Sohal, Mark Holtz, Marauo Davis, Louisa J. Hope-Weeks, and Jharna Chaudhuri. Synthesis and photoluminescence properties of hierarchical architectures of YBO_3:Eu^{3+}. *J. Mater. Chem.*, 22(13):6485, 2012.

[25] JinDeng Chen, Hai Guo, ZhengQuan Li, Hao Zhang, and YiXi Zhuang. Near-infrared quantum cutting in Ce^{3+}, Yb^{3+} co-doped YBO_3 phosphors by cooperative energy transfer. *Optical Materials*, 32(9):998–1001, July 2010.

[26] Wei, Sun, Liao, Yin, Jiang, Yan, and Shaozhe Lü. Size-dependent chromaticity in YBO_3:Eu nanocrystals: correlation with microstructure and site symmetry. *J. Phys. Chem. B*, 106(41):10610–10617, October 2002.

[27] K W Kramer, P Dorenbos, H U Gudel, and C W E van Eijk. Development and characterization of highly efficient new cerium doped rare earth halide scintillator materials. *J. Mater. Chem.*, 16(27):2773, 2006.

[28] R A Hansel, S W Allison, and D G Walker. Temperature-dependent luminescence of gallium-substituted YAG:Ce. *J Mater Sci*, 45(1):146, 2009.

[29] Ling Li, Shihong Zhou, and Siyuan Zhang. Crystal structure and charge transfer energy of the vaterite-type orthoborate YBO_3:Eu. *Solid State Sciences*, 10(9):1173–1178, September 2008.

[30] J B Birks and F A Black. Deterioration of anthracene under α-particle irradaition. *Proceedings of the Physical Society A*, 64:511–512, 1951.

[31] Prashant K Sharma, Ranu K Dutta, and Avinash C Pandey. Size dependence of Eu-O charge transfer process on luminescence characteristics of YBO_3:Eu^{3+} nanocrystals. *Optics letters*, 35(14):2331–2333, 2010.

[32] S M Goedeke, W A Hollerman, S W Allison, P A Gray, L A Lewis, R W Smithwick, L A Boatner, D C Glasgow, R S Fontenot, and H Wise. Comparison of Cathodoluminescent and Photoluminescent Emission Spectra of ¡formula formulatype="inline"¿¡tex¿$LuPO_4$¡/tex¿¡/formula¿ With Europium, Erbium, and Neodymium Dopants. *IEEE Trans. Nucl. Sci.*, 55(3):1107–1110, June 2008.

[33] W A Hollerman, R F Guidry, F N Womack, N P Bergeron, S W Allison, S M Goedeke, D L Beshears, M R Cates, T J Bencic, and C R Mercer. Use of phosphor coatings for high temperature aerospace applications. 2003.

[34] W A Hollerman, S M Goedeke, R J Moore, L A Boatner, S W Allison, and R S Fontenot. Unusual fluorescence emission characteristics from europium-doped lead phosphate glass caused by 3 mev proton irradiation. In *Nuclear Science Symposium Conference Record, 2007. NSS '07. IEEE*, pages 1368–1372, 2007.

[35] L R Holland, G M Jenkins, J H Fisher, W A Hollerman, and G A Shelby. Efficiency and radiation hardness of phosphors in a proton beam. *Nuclear Instruments and Methods in Physics Research Section B*, 56:1239–1241, May 1991.

[36] W A Hollerman, J H Fisher, G A Shelby, L R Holland, and G M Jenkins. Proton damage measurements of rare earth oxide scintillators. In *Nuclear Science Symposium, 1990. Conference record : Including Sessions on Nuclear Power Systems and Medical Imaging Conference, 1990 IEEE*, pages 892–895. IEEE, 1990.

[37] W A Hollerman, J H Fisher, G A Shelby, L R Holland, and G M Nuclear Science IEEE Transactions on Jenkins. Spectroscopic analysis of proton-induced fluorescence from yttrium and gadolinium oxysulfide phosphors. *IEEE Trans. Nucl. Sci.*, 39(6).

[38] W A Hollerman, J H Fisher, L R Holland, and J B Czirr. Spectroscopic analysis of proton-induced fluorescence from yttrium orthosilicate. *IEEE Trans. Nucl. Sci.*, 40(5):1355–1358, 1993.

[39] W A Hollerman, J H Fisher, L R Holland, G M Jenkins, D B Nisen, E K Williams, and C C Foster. Measurement of fluorescence phenomena from yttrium and gadolinium fluors using a 45 MeV proton beam. *Nuclear Instruments and Methods in Physics Research Section A: Accelerators, Spectrometers, Detectors and Associated Equipment*, 353(1):20–23, 1994.

[40] E Gaubas, I Brytavskyi, T Ceponis, A Jasiunas, V Kalesinskas, V Kovalevskij, D Meskauskaite, J Pavlov, V Remeikis, G Tamulaitis, and A Tekorius. In situ variations of carrier decay and proton induced luminescence characteristics in polycrystalline CdS. *J. Appl. Phys.*, 115(24):243507, June 2014.

[41] V Kortov. Modern trends and development in high-dose luminescent measurements. *J. Phys.: Conf. Ser.*, 552(1):012039–8, November 2014.

[42] T Hirouchi, M Nishiura, T Nagasaka, T Ido, D Funaki, T Kobuchi, A Okamoto, S Kitajima, M Sasao, K Fujioka, M Isobe, and T Mutoh. Effect of ion beam and neutron irradiations on the luminescence of polycrystalline Ce-doped $Y_3Al_5O_{12}$ ceramics. *Journal of Nuclear Materials*, 386-388(C):1049–1051, April 2009.

[43] A V Gektin, N V Shiran, and V V Voronova. Radiation damage in pure and rare earth doped $LiBaF_3$ crystals. *IEEE Trans. Nucl. Sci.*, 44(3):857–860, 1997.

[44] V G Baryshevsky, M V Korzhik, V I Moroz, V B Pavlenko, A A Fyodorov, S A Smirnova, O A Egorycheva, and V A Kachanov. $YAlO_3$:Ce-fast-acting scintillators for detection of ionizing radiation. *Nuclear Inst. and Methods in Physics Research, B*, 58:291–293, 1991.

[45] T Bücherl, C Rausch, and H von Seggern. Quantitative measurements on thermal neutron detectors based on storage phosphors. *Nuclear Instruments and Methods in Physics Research Section A: Accelerators, Spectrometers, Detectors and Associated Equipment*, 333(2):502–506, 1993.

[46] G A Appleby, A Edgar, G V M Williams, and A J J Bos. Photostimulated luminescence from $BaCl_2$:Eu^{2+} nanocrystals in lithium borate glasses following neutron irradiation. *Appl. Phys. Lett.*, 89(10):101902, 2006.

[47] K Sakasai, M Katagiri, M Matsubayashi, T Nakamura, and Y Kondo. Characteristics of $SrBPO_5$:Ce^{3+} based materials as a neutron storage phosphor. *Nuclear Instruments and Methods in Physics Research Section A: Accelerators, Spectrometers, Detectors and Associated Equipment*, 529(1-3):378–383, August 2004.

[48] D Solodovnikov, M H Weber, D T Haven, and K G Lynn. Single crystal ce doped scintillator material with garnet structure sensitive to gamma ray and neutron radiation. *Journal of Crystal Growth*, 352(1):99–102, August 2012.

[49] Masaaki Kobayashi, Masaharu Ieiri, Kenjiro Kondo, Taichi Miura, Hiroyuki Noumi, Masaharu Numajiri, Yuichi Oki, Takenori Suzuki, Minoru Takasaki, Kazuhiro Tanaka, Yutaka Yamanoi, and Mitsuru Ishii. Radiation hardness of cerium-doped gadolinium silicate Gd_2SiO_5:Ce against high energy protons, fast and thermal neutrons. *Nuclear Instruments and Methods in Physics Research Section A: Accelerators, Spectrometers, Detectors and Associated Equipment*, 330(1-2):115–120, 1993.

[50] P F Hinrichse, A J Houdayer, A L Barry, and J Vincent. Proton induced damage in SiC light emitting diodes. *IEEE Trans. Nucl. Sci.*, 45(6):2808–2812, December 1998.

[51] C Carlone, M Parenteau, A Houdayer, P Hinrichsen, and J Vincent. Photoluminescence study of gallium vacancy defects in gallium arsenide irradiated by relativistic protons. *IEEE Transactions on Nuclear Science*, 44(6):1856–1861, December 1997.

[52] A L Barry, A J Houdayer, P F Hinrichsen, W G Letourneau, and J Vincent. The energy dependence of lifetime damage constants in GaAs LEDs for 1-500 MeV protons. *IEEE Transactions on Nuclear Science*, 42(6):2104–2107, December 1995.

[53] Zhi-Yi Zhang, K T V Grattan, A W Palmer, and B T Meggitt. Thulium-doped intrinsic fiber optic sensor for high temperature measurements ($> 1100^{\circ}$C). *Review of Scientific Instruments*, 69(9):3210–6, 1998.

[54] M Yu, G Särner, C C M Luijten, M Richter, M Aldén, R S G Baert, and L P H de Goey. Survivability of thermographic phosphors (YAG:Dy) in a combustion environment. *Measurement Science and Technology*, 21(3):037002–5, February 2010.

[55] John B Gruber, Michael D Seltzer, Marian E Hills, Sally B Stevens, and Clyde A Morrison. Energy levels and upconversion fluorescence in trivalent thulium-doped yttrium scandium aluminum garnet. *J. Appl. Phys.*, 73(4):1929–8, 1993.

[56] S Guy, M Malinowski, Z Frukacz, M F Joubert, and B Jacquier. Dynamics of the high lying excited states of Tm^{3+} ions in YAG. *Journal of Luminescence*, 68(2-4):115–127, 1996.

[57] Z Y Zhang, K T V Grattan, and B T Meggitt. Thulium-doped fiber optic decay-time temperature sensors: Characterization of high temperature performance. *Review of Scientific Instruments*, 71(4):1614–8, 2000.

[58] D L Dexter. A theory of sensitized luminescence in solids. *J. Chem. Phys.*, 21(5):836, 1953.

[59] S L Weeden-Wright, S L Gollub, R Harl, A B Hmelo, D M Fleetwood, B R Rogers, R D Schrimpf, and D G Walker. Radiation effects on the photoluminescence of rare-earth doped pyrochlore powders. *IEEE Transactions on Nuclear Science*, 60(4):2444–2449.

[60] N T Melamed. Optical Properties of Powders. Part I. Optical Absorption Coefficients and the Absolute Value of the Diffuse Reflectance. Part II. Properties of Luminescent Powders. *J. Appl. Phys.*, 34(3):560, 1963.

[61] G Chadeyron, R Mahiou, M El-Ghozzi, A Arbus, D Zambon, and J C Cousseins. Luminescence of the orthoborate YBO_3:Eu^{3+}. relationship with crystal structure. *Journal of Luminescence*, 72–74:564–566, 1997.

[62] G Chadeyron, M El-Ghozzi, R Mahiou, A Arbus, and J C Cousseins. Revised structure of the orthoborate YBO_3. *Journal of Solid State Chemistry*, 128(2):261–266, 1997.

[63] H M Kriz. On the crystal structure of YBO_3, a vaterite-type borate. *J. Chem. Phys.*, 51(8):3624, 1969.

[64] S. L. Gollub, R. R. Harl, S. L. Weeden-Wright, B. R. Rogers, and D. G. Walker. Phosphors as sensors for radiation-induced displacement damage. In *Symposium YY Rare-Earth-Based Materials*, volume 1471 of *MRS Proceedings*, 2012.

[65] J F Ziegler, J P Biersack, and U Littmark. *The stopping and range of ions in solids*. Pergamon Press, New York, 1985.

[66] Hiroko Ogata, Satoru Takeshita, Tetsuhiko Isobe, Tomohiro Sawayama, and Seiji Niikura. Factors for determining photoluminescence properties of YBO_3:Ce^{3+} phosphor prepared by hydrothermal method. *Optical Materials*, 33(11):1820–1824, September 2011.

[67] R I Smirnova, Y S Blank, and T Y Rumyantseva. The dependence of the cathodeluminescence properties of YBO_3:Ce on the concentration of cerium. *Journal of Applied Spectroscopy*, 15(3):1169–1172, 1971.

[68] M J Knitel, P Dorenbos, CWE Van Eijk, B Plasteig, B Viana, A Kahn-Harari, and D Vivien. Photoluminescence, and scintillation/thermoluminescence yields of several Ce^{3+} and Eu^{2+} activated borates. *Nuclear Instruments and Methods in Physics Research Section A: Accelerators, Spectrometers, Detectors and Associated Equipment*, 443(2):364–374, 2000.

[69] Xiao-Cheng Jiang, Chun-Hua Yan, Ling-Dong Sun, Zheng-Gui Wei, and Chun-Sheng Liao. Hydrothermal homogeneous urea precipitation of hexagonal YBO_3:Eu^{3+} nanocrystals with improved luminescent properties. *Journal of Solid State Chemistry*, 175(2):245–251, November 2003.

[70] Peter D Johnson and Ferd E Williams. The Interpretation of the Dependence of Luminescent Efficiency on Activator Concentration. *J. Chem. Phys.*, 18(11):1477, 1950.

[71] Herbert B. Rosenstock and James H. Schulman. Models for luminescence degradation in organic solids. *Journal of Chemical Physics*, 30(1):116–125, January 1959.

[72] D L Dexter and James H Schulman. Theory of concentration quenching in inorganic phosphors. *Journal of Chemical Physics*, 22(6):1063–1070, 1954.

[73] L.M. Wang, L.Q. Zhuang, H. Xin, Y.X. Huang, and D.Q. Wang. Semi-quantitative estimation of Ce^{3+}/Ce^{4+} ratio in YAG:Ce^{3+} phosphor under different sintering atmosphere. *Open Journal of Inorganic Chemistry*, 5:12–18, January 2015.

[74] Guang Jia, Hongpeng You, Kai Liu, Yuhua Zheng, Ning Guo, Junjiao Jia, and Hongjie Zhang. Highly uniform YBO_3 hierarchical architectures: Facile synthesis and tunable luminescence properties. *Chem. Eur. J.*, 16(9):2930–2937, January 2010.

[75] Akihiro Nohara, Satoru Takeshita, and Tetsuhiko Isobe. Mixed-solvent strategy for solvothermal synthesis of well-dispersed YBO_3:Ce^{3+},Tb^{3+} nanocrystals. *RSC Adv.*, 4(22):11219, 2014.

[76] Xiao-Cheng Jiang, Ling-Dong Sun, and Chun-Hua Yan. Ordered nanosheet-based YBO_3:Eu^{3+} assemblies: synthesis and tunable luminescent properties. *J. Phys. Chem. B*, 108(11):3387–3390, March 2004.

[77] Yusuke Kamiyama, Takehiko Hiroshima, Tetsuhiko Isobe, Toru Koizuka, and Suguru Takashima. Photostability of YAG:Ce^{3+} nanophosphors synthesized by glycothermal method. *J. Electrochem. Soc.*, 157(5):J149–J154, 2010.

[78] Hiroki Hara, Satoru Takeshita, Tetsuhiko Isobe, Yasushi Nanai, Tsuyoshi Okuno, Tomohiro Sawayama, and Seiji Niikura. Glycothermal synthesis and photoluminescent properties of Ce^{3+}-doped YBO_3 mesocrystals. *Journal of Alloys and Compounds*, 577:320–326, November 2013.

[79] Yuntao Wu, Guohao Ren, Dongzhou Ding, Fan Yang, and Shangke Pan. Study on the cerium oxidation state in a $Lu_{0.8}Sc_{0.2}BO_3$ host. *J. Mater. Chem.*, 21(44):17805–17809, 2011.

[80] L J Curtis, H G Berry, and J Bromander. Analysis of multi-exponential decay curves. *Physica Scripta*, 2(4-5):216–220, October 1970.

[81] A H Khalid and K Kontis. Progress towards absolute intensity measurements of emissions from high temperature thermographic phosphors. *Journal of Luminescence*, 131(7):1312–1321, July 2011.